KIDNEY DISEASE

Modeling injury and repair in kidney organoids reveals that homologous recombination governs tubular intrinsic repair

Navin Gupta[1,2,3,4]†, Takuya Matsumoto[1,2,4]†, Ken Hiratsuka[1,2,4,5]†, Edgar Garcia Saiz[2,4], Pierre Galichon[3,4,6], Tomoya Miyoshi[4], Koichiro Susa[4], Narihito Tatsumoto[7], Michifumi Yamashita[7], Ryuji Morizane[1,2,3,4,5]*

Kidneys have the capacity for intrinsic repair, preserving kidney architecture with return to a basal state after tubular injury. When injury is overwhelming or repetitive, however, that capacity is exceeded and incomplete repair results in fibrotic tissue replacing normal kidney parenchyma. Loss of nephrons correlates with reduced kidney function, which defines chronic kidney disease (CKD) and confers substantial morbidity and mortality to the worldwide population. Despite the identification of pathways involved in intrinsic repair, limited treatments for CKD exist, partly because of the limited throughput and predictivity of animal studies. Here, we showed that kidney organoids can model the transition from intrinsic to incomplete repair. Single-nuclear RNA sequencing of kidney organoids after cisplatin exposure identified 159 differentially expressed genes and 29 signal pathways in tubular cells undergoing intrinsic repair. Homology-directed repair (HDR) genes including Fanconi anemia complementation group D2 (*FANCD2*) and RAD51 recombinase (*RAD51*) were transiently up-regulated during intrinsic repair but were down-regulated in incomplete repair. Single cellular transcriptomics in mouse models of obstructive and hemodynamic kidney injury and human kidney samples of immune-mediated injury validated HDR gene up-regulation during tubular repair. Kidney biopsy samples with tubular injury and varying degrees of fibrosis confirmed loss of FANCD2 during incomplete repair. Last, we performed targeted drug screening that identified the DNA ligase IV inhibitor, SCR7, as a therapeutic candidate that rescued FANCD2/RAD51-mediated repair to prevent the progression of CKD in the cisplatin-induced organoid injury model. Our findings demonstrate the translational utility of kidney organoids to identify pathologic pathways and potential therapies.

INTRODUCTION

Chronic kidney disease (CKD) is a global health problem of high economic cost to health care systems, affecting up to 13.4% of the population worldwide (*1*). Repeated acute kidney injury (AKI) promotes the onset and progression of CKD (*2*). Kidney tubular cells may undergo repair after acute injury. Injured proximal tubules are thought to be repaired through terminally differentiated epithelia reexpressing kidney developmental markers during injury-induced dedifferentiation and proliferation, because lineage tracing studies have not identified a nephron progenitor population in adults (*3*, *4*). Dedifferentiation and proliferation represent intrinsic repair processes that preserve tubular architecture. Conversely, severe or recurrent tubular injury induces failed repair associated with epithelial G_2-M cell cycle arrest, tubular atrophy, myofibroblast transdifferentiation, and interstitial fibrosis (*5*–*11*). Animal studies have identified processes involved in tubular injury and repair, identifying potential therapeutic pathways such as bone morphogenic protein, Wnt, NOTCH, and hypoxia inducible factor signaling (*12*, *13*). However, translating animal studies into clinical settings has been difficult because many treatments deemed safe and effective in animals have subsequently been found to be nephrotoxic or ineffective in clinical trials (*14*). Development of human cell-based tools may therefore be an important addition to current methodologies, including animal studies, used during drug development.

Advances in stem cell biology have enabled the generation of kidney organoids from human pluripotent stem cells (hPSCs) (*15*–*17*). Kidney organoid technology is rapidly evolving and has demonstrated utility in simulating kidney development, nephrotoxicity, and kidney diseases (*15*, *18*, *19*). We and others have used kidney organoids to study kidney fibrotic responses (*20*, *21*). These studies led us to hypothesize that organoids may be used to study tubular injury and repair processes, including the conversion from intrinsic to failed repair.

RESULTS

Multicompartment kidney organoids differentiate over time to model AKI

Kidney organoids were generated using our previously published protocol that subdivided kidney organogenesis into distinct intermediate stages (*15*, *18*). The protocol simultaneously induced SIX homeobox 2^+ ($SIX2^+$) nephron progenitor cells (NPCs) and $SIX2^-$ Meis homeobox 1^+ ($MEIS1^+$) stromal progenitor cells (SPCs) at the metanephric mesenchyme stage (Fig. 1A and fig. S1, A and B) (*16*, *22*) that subsequently differentiated into nephrons and interstitial cells including PDGFR-β^+NG2$^-$DESM$^-$ fibroblasts and perivascular PDGFR-β^+NG2$^+$DESM$^+$ pericytes (Fig. 1B and fig. S1C)

[1]Nephrology Division, Department of Medicine, Massachusetts General Hospital, Boston, MA 02114, USA. [2]Harvard Medical School, Boston, MA 02115, USA. [3]Harvard Stem Cell Institute (HSCI), Cambridge, MA 02138, USA. [4]Renal Division, Department of Medicine, Brigham and Women's Hospital, Boston, MA 02115, USA. [5]Wyss Institute for Biologically Inspired Engineering, Harvard University, Boston, MA 02115, USA. [6]Sorbonne Université, INSERM UMR-S1155, Paris, France. [7]Department of Pathology and Laboratory Medicine, Cedars-Sinai Medical Center, Los Angeles, CA 90048, USA.
*Corresponding author. Email: rmorizane@mgh.harvard.edu
†These authors contributed equally to this work.

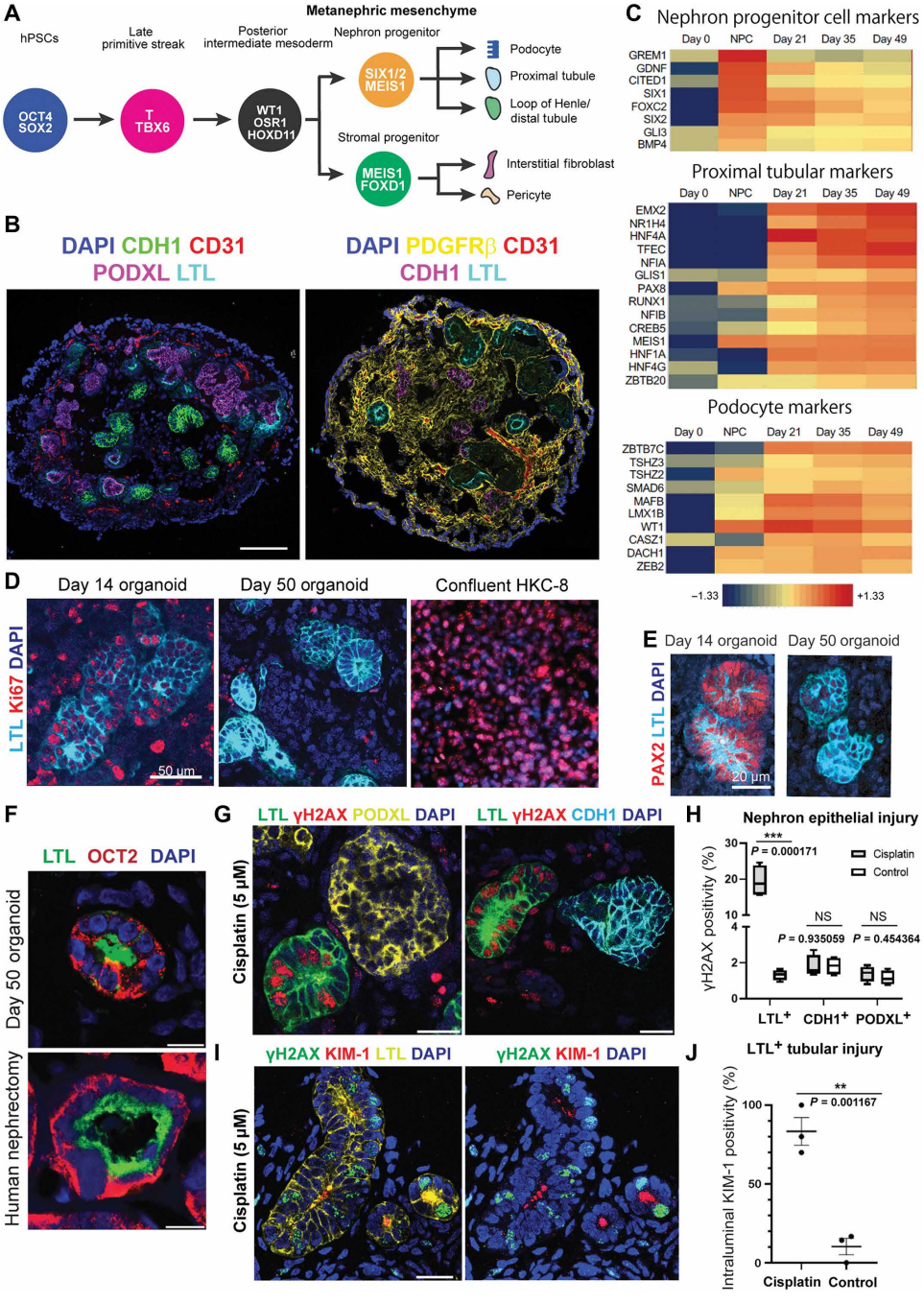

Fig. 1. hPSC-derived metanephric mesenchyme cells contain nephron and SPCs and develop into multicompartment kidney organoids that mature over time. (**A**) Differentiation protocol for kidney organoids. (**B**) Immunostaining of markers of nephrons (PODXL, LTL, and CDH1) and stroma (CD31 and PDGFR-β) markers in kidney organoids. Scale bar, 100 μm. (**C**) Heatmap of bulk RNA-seq for markers of nephron progenitors (top), proximal tubules (middle), and podocytes (bottom) over time. (**D**) LTL and Ki67 immunostaining in developing and developed kidney organoids, as compared to immortalized proximal tubules. Scale bar, 50 μm. (**E**) PAX2 immunostaining in LTL^+ cells in kidney organoids over time. Scale bar, 20 μm. (**F**) OCT2 and LTL immunostaining in developed kidney organoids, as compared to human nephrectomy. Scale bars, 25 μm. (**G**) γH2AX immunostaining across nephron segments. Scale bars, 50 μm. (**H**) Quantification of $γH2AX^+$ in nephron segments. $n = 4$ sections of three independent organoids from two independent experiments (a total of 5166 LTL^+, 5091 $PODXL^+$, and 1854 $CDH1^+$ cells were counted). Cisplatin versus control in LTL^+ was $P = 1.71 \times 10^{-4}$, $CDH1^+$ was $P = 0.935$, and $PODXL^+$ was $P = 0.454$. (**I**) KIM-1 and γH2AX immunostaining in LTL^+ structures after cisplatin. Scale bar, 50 μm. (**J**) $KIM\text{-}1^+$ in LTL^+ tubules after cisplatin.2-independent experiments each using three organoids with 52 LTL^+ structures counted. Cisplatin versus control, $P = 1.167 \times 10^{-3}$. $^{**}P < 0.01$ and $^{***}P < 0.001$. NS, not significant.

(*23*, *24*). Immunostaining of SIX1 demonstrated a similar distribution to SIX2 (fig. S1B), consistent with overlapping SIX1 and SIX2 activity in human fetal NPCs because an autoregulatory loop drives dual expression (*25*). Concurrent flow cytometric analysis of SIX2 and MEIS1 expression confirmed the induction of SIX2 in 87.7% of cells, whereas 22.4% of the $SIX2^-$ fraction expressed MEIS1, consistent with the simultaneous induction of NPCs and SPCs (fig. S1D). Our results indicated that >99% of hPSC-derived $SIX2^+$ cells were positive for MEIS1 (fig. S1E), consistent with human embryonic kidney in vivo (*22*, *26*). The classical kidney stromal progenitor marker, forkhead box D1 (FOXD1), was apparent in the $SIX2^-$ population of metanephric mesenchyme (fig. S1F), with mRNA expression peaking on day 21 followed by up-regulation of the fibroblast marker *CD73*, suggesting maturation from an SPC pool (fig. S1G). Organoid development was evaluated for the loss of developmental genes and the induction of mature markers such as SIX1 and empty spiracles homeobox 2 (EMX2) (*27*, *28*). Bulk RNA sequencing (RNA-seq) of developing organoids demonstrated transient induction of kidney developmental markers (Fig. 1C, top), whereas up-regulated expression of adult kidney genes was consistent with proximal tubular and podocyte differentiation (Fig. 1C, middle and bottom). Comparative bulk transcriptomic analysis suggested that, at days 35, 49, and 63, organoids progressively matured and most closely resembled second trimester kidney (fig. S2), but discordant results between differing datasets of fetal 9-, 16-, 18-, and 22-week human kidney suggested heterogeneity arising from sample preparation. Loss of the cell cycle marker Ki67 was indicative of tubular maturation toward terminally differentiated counterparts in vivo (*3*), whereas the Human kidney cell clone 8 (HKC-8) tubular epithelial cell line displayed persistent cell cycle activity (Fig. 1D). Reduced expression of developmental genes, such as *PAX2* (Fig. 1E), up-regulated expression of adult markers such as EMX2 and zinc finger and BTB domain containing 7C (ZBTB7C) (Fig. 1C, middle and bottom), and exit from the cell cycle

(Fig. 1D) reflected maturation of kidney organoids over time. Because polarity is a reported sign of functional tubular maturation (*29*), we assessed organoids to locate apical multidrug resistance-1, basolateral Na-K adenosine triphosphatase, and circumferential aquaporin-1 and organic cation transporter 2 (OCT2) in *Lotus tetragonolobus* lectin$^+$ (LTL$^+$) proximal tubules (fig. S3, A to C).

AKI is a complication of cisplatin therapy for the treatment of solid organ tumors, occurring in 20 to 30% of patients (*30*). Cisplatin nephrotoxicity is cumulative and dose dependent (*31*), with the proximal tubule demonstrating the greatest sensitivity to injury because it aids in cisplatin excretion (*32*). OCT2 is one of the major transporters that mediates basolateral influx of cisplatin (*30*, *33*), coupled to apical efflux via multidrug and toxin extrusion proteins 1 and 2K (MATE1 and MATE2K) (fig. S4A). Greater OCT2 transport activity than MATE1/2K leads to intracellular cisplatin accumulation and nephrotoxicity in vivo (*34*). hPSC-derived kidney organoids expressed the genes of OCT2, MATE1, and MATE2K (fig. S4B). Immunostaining of OCT2 and LTL, in day 50 organoids, was similar to adult human kidney controls (Fig. 1F). Treatment with low-concentration cisplatin (5 μM) induced double-stranded DNA breaks (DSBs) with expression of γ H2A histone family member X (γH2AX) (*35*) in LTL$^+$ tubules while sparing podocalyxin (PODXL) and E-cadherin (CDH1)–positive podocyte and distal tubular cells, as well as the collective non-LTL cells (Fig. 1, G and H, and fig. S4C). The proximal tubule–specific injury marker, kidney injury marker-1 (KIM-1) (*2*), was manifested by 83.1 ± 9.0% of LTL$^+$ tubules after cisplatin treatment compared to 10.3 ± 5.2% in controls (Fig. 1, I and J, and fig. S4D). Quantification of KIM-1 in controls did not differ from samples stained with the secondary antibody alone, consistent with nonspecific brush border staining (fig. S4, E and F). The specificity of the proximal tubule for cisplatin-related injury demonstrated the utility of stem cell–derived kidney organoids for modeling AKI.

Proximal tubules exhibit intrinsic repair responses with preserved tubular architecture over time after cisplatin treatment

Injured proximal tubular cells proliferate to replace injured counterparts and maintain tubular integrity (*3*, *5*). Early features of the tubular cells' intrinsic response to injury include cell cycle entry and dedifferentiation with returned expression of developmental genes (*6*, *36*, *37*). Consistent with mammalian models in vivo, developing LTL$^+$ tubules in organoids expressed the developmental markers SRY-box transcription factor 9 (SOX9) and paired box 2 (PAX2), with the latter lost during proximal tubular maturation and reactivated after injury as descendant cells regenerated functional proximal tubules (Figs. 1E and 2A and fig. S5, A and B) (*3*, *38*). Injured LTL$^+$ cells exhibited vimentin (VIM), a mesenchymal marker characteristic of partial epithelial-to-mesenchymal transition (pEMT) (Fig. 2B) (*9*, *39*). DNA-damaged proximal tubules (γH2AX$^+$LTL$^+$) demonstrated the strongest expression of VIM, consistent with proximal tubular DNA damage catalyzing mesenchymal transformation (*6*). Homology-directed repair (HDR) or nonhomologous end joining (NHEJ) is a predominant mechanism by which DNA is repaired (*40*). DNA-damaged LTL$^+$ cells demonstrated about threefold up-regulation in the abundance of the HDR protein, FANCD2, compared to controls (Fig. 2, C and D, and fig. S6) (*41*).

We presumed that resolved DNA damage, tubular cell exit from the cell cycle, and preservation of tubular architecture represented intrinsic repair. After cisplatin injury, we monitored for intrinsic repair (Fig. 2E). By day 7 after injury, LTL$^+$ cells had reduced expression of γH2AX and exited the cell cycle while retaining tubular morphology (Fig. 2, F to H). Similarly, quantitative polymerase chain reaction (qPCR) of *H2AFX* and *Ki67* indicated resolution of DNA damage and reduced cell cycle activity (Fig. 2, I and J). In response to a single treatment with low-dose cisplatin, proximal tubules demonstrated intrinsic repair over time with HDR activation for the resolution of DNA damage.

Proximal tubules exhibit incomplete repair responses associated with tubular atrophy after repeated cisplatin treatment

Tubular incomplete repair is a consequence of failed recovery after repetitive AKI (*42*). Repeated administration of low-concentration cisplatin (5 μM) and diphtheria toxin–targeted proximal tubular injury trigger incomplete repair in mice (*43*, *44*). The induction of profibrotic phenotypes in proximal tubules drives kidney fibrosis in the absence of leukocyte infiltration or inflammation in mice (*45*), providing proof of concept to simulate incomplete repair in kidney organoids. Whereas a single cisplatin injury in organoids stimulated intrinsic repair, we hypothesized that repeated injury may induce incomplete repair characterized by histologic changes of tubular atrophy and interstitial fibrosis. Organoids were therefore subjected to twice weekly cisplatin during weeks 8 and 9 of differentiation (Fig. 3A). LTL$^+$ tubules increasingly entered the cell cycle with repeated cisplatin administration (Fig. 3, B and C), with about 30% expressing the active cell cycle marker, Ki67 (*46*), after the third treatment. Stalling or arresting in the G_2-M phase of the cell cycle is a well-described phenotype of tubular incomplete repair (*8*). After the fourth cisplatin treatment, flow cytometry of live LTL$^+$ cells for DNA content demonstrated a 2.4-fold increase in tetraploid cells, consistent with G_2-M arrest (fig. S7, A and B). Tubules became fragmented, signifying the transition from intrinsic to incomplete repair (Fig. 3B) (*47*). After the fifth cisplatin treatment, histologic analysis displayed organoid atrophy with >2-fold reduction in cross-sectional area and tubular number (Fig. 3, D and E). Pathophysiology of the human kidney in vivo has demonstrated a similar association between kidney size and tubular atrophy (*48*, *49*). Between the fourth and fifth cisplatin treatment, PDGFR-β$^+$ stroma lost expression of phosphatase and tensin homolog (PTEN) (Fig. 3F), which protects against tubular atrophy and fibrosis during AKI (*50*), and demonstrated a 10-fold up-regulation of the myofibroblast marker, α–smooth muscle actin (αSMA) (Fig. 3, F and G). The transition to incomplete repair phenotypes of tubular atrophy and myofibroblast activation was preceded by up-regulation of the proinflammatory cytokine, *CTGF* (fig. S7C). Upon further investigation, αSMA$^+$PDGFR-β$^+$ cells surrounding tubular structures lacked the pericyte marker, neuron glial antigen 2 (NG2), whereas nonperitubular αSMA$^+$PDGFR-β$^+$ cells coexpressed NG2 (Fig. 3H), suggesting that peritubular fibroblasts and pericytes served as sources of myofibroblasts in organoids, consistent with a recent study of human kidney samples with single-cell RNA-seq (scRNA-seq) and assay for transposase-accessible chromatin using sequencing (ATAC-seq) (*51*).

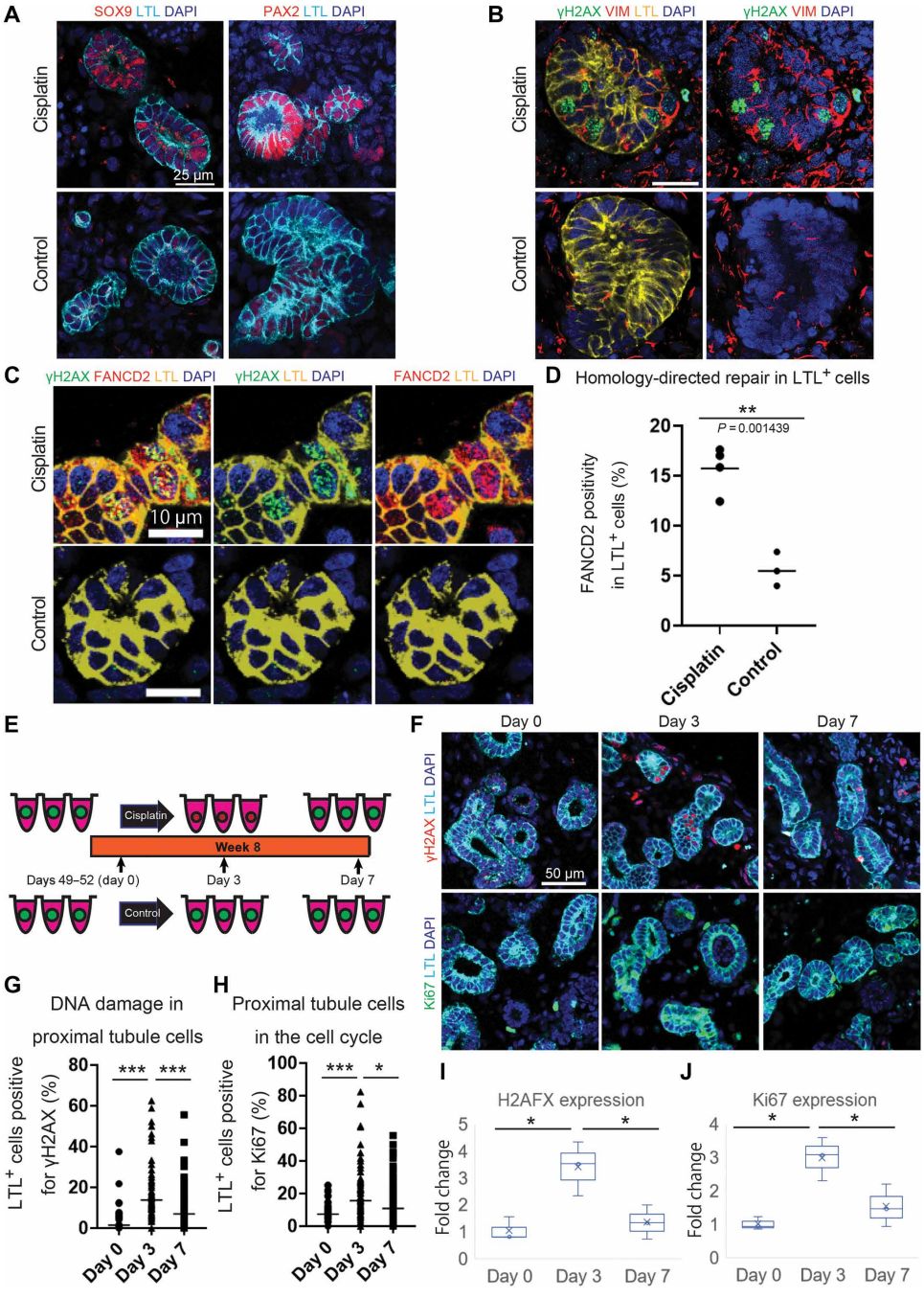

Fig. 2. Proximal tubules exhibit intrinsic repair with preserved tubular architecture over time after cisplatin treatment. (**A**) SOX9 and PAX2 immunostaining in LTL$^+$ cells with and without cisplatin. Scale bar, 25 μm. (**B**) VIM immunostaining in LTL$^+$ cells with and without cisplatin. Scale bar, 25 μm. (**C**) γH2AX and FANCD2 immunostaining in LTL$^+$ cells with and without cisplatin. Scale bars, 10 μm. (**D**) Quantification of FANCD2$^+$ in LTL$^+$ cells with and without cisplatin. Data points reflect the mean of three organoids per sample in each of three independent experiments (a total of 971 cisplatin-treated LTL$^+$ cells and 1133 untreated LTL$^+$ cells were counted). Cisplatin versus control, $P = 1.439 \times 10^{-3}$. (**E**) Protocol to monitor for intrinsic repair. (**F**) γH2AX and Ki67 immunostaining in LTL$^+$ cells over time after cisplatin. Scale bar, 50 μm. (**G** and **H**) Quantification of γH2AX$^+$ and Ki67$^+$ in LTL$^+$ cells over time after cisplatin. Each data point reflecting results of a single organoid across three independent experiments (γH2AX: day 0 versus day 3 with $P = 4.772 \times 10^{-6}$ and day 3 versus day 7 with $P = 6.883 \times 10^{-3}$, $n = 3$ to 6 organoids across three independent experiments; Ki67: day 0 versus day 3 with $P = 2.282 \times 10^{-14}$ and day 3 versus day 7 with $P = 4.087 \times 10^{-6}$). (**I** and **J**) Reverse transcription qPCR (RT-qPCR) of *H2AFX* and *Ki67* over time after cisplatin (γH2AX: day 0 versus day 3 with $P = 0.0203$ and day 3 versus day 7 with $P = 0.0403$; Ki67: day 0 versus day 3 with $P = 0.0500$ and day 3 versus day 7 with $P = 7.087 \times 10^{-3}$). $^*P < 0.05$, $^{**}P < 0.01$, and $^{***}P < 0.001$.

Loss of HDR gene expression in injured tubular cells correlates with the induction of incomplete repair

After repeated cisplatin injury, induction of tubular atrophy and αSMA$^+$PDGFR-β$^+$ myofibroblasts was associated with an acute reduction of the HDR protein FANCD2 (Fig. 4A) despite progressively increased tubular DNA damage (Fig. 4B). The expression of FANCD2 in γH2AX$^+$ LTL$^+$ cells reduced from about 90 to <50% (Fig. 4C). Confirmatory qPCR of the HDR genes, *BRCA2*, *RAD51*, and *RPA1*, demonstrated increased expression during intrinsic repair and reduced expression below controls during incomplete repair (Fig. 4D); conversely, NHEJ genes, *KU80*, *XRCC4*, and *LIG4*, displayed unchanged expression (Fig. 4E). Loss of HDR gene expression correlated with a transition from intrinsic to incomplete repair; hence, we hypothesized that DNA-damaged tubules in fibrotic human kidney biopsy samples might lack FANCD2 expression. To test this hypothesis, we compared three groups of kidney diseases: minimal change disease (MCD), MCD with acute tubular injury (MCD w/ ATN), and diabetic glomerulosclerosis (DGS) with moderate interstitial fibrosis/tubular atrophy (IFTA). MCD w/ ATN samples exhibited increased γH2AX and FANCD2 in LTL$^+$ proximal tubules, suggesting intrinsic repair, whereas FANCD2 was reduced in DNA-damaged proximal tubules in DGS with IFTA samples (Fig. 4, F and G). Analysis of biopsy samples and clinical data suggested an inverse correlation between serum creatinine and FANCD2 abundance in injured tubules (fig. S8). These results suggested the importance of HDR for intrinsic repair after tubular injury.

Single nuclear RNA-seq reveals injury clusters with HDR gene activity during intrinsic repair

Single nuclear RNA-seq (snRNA-seq) of kidney organoids corresponding to control, cisplatin ×3, and cisplatin ×5 was conducted to evaluate transcriptional changes during the transition from intrinsic to incomplete repair, overcoming the loss of cell-specific information in prior qPCR that may obscure changes in target populations. We chose snRNA-seq to limit RNA

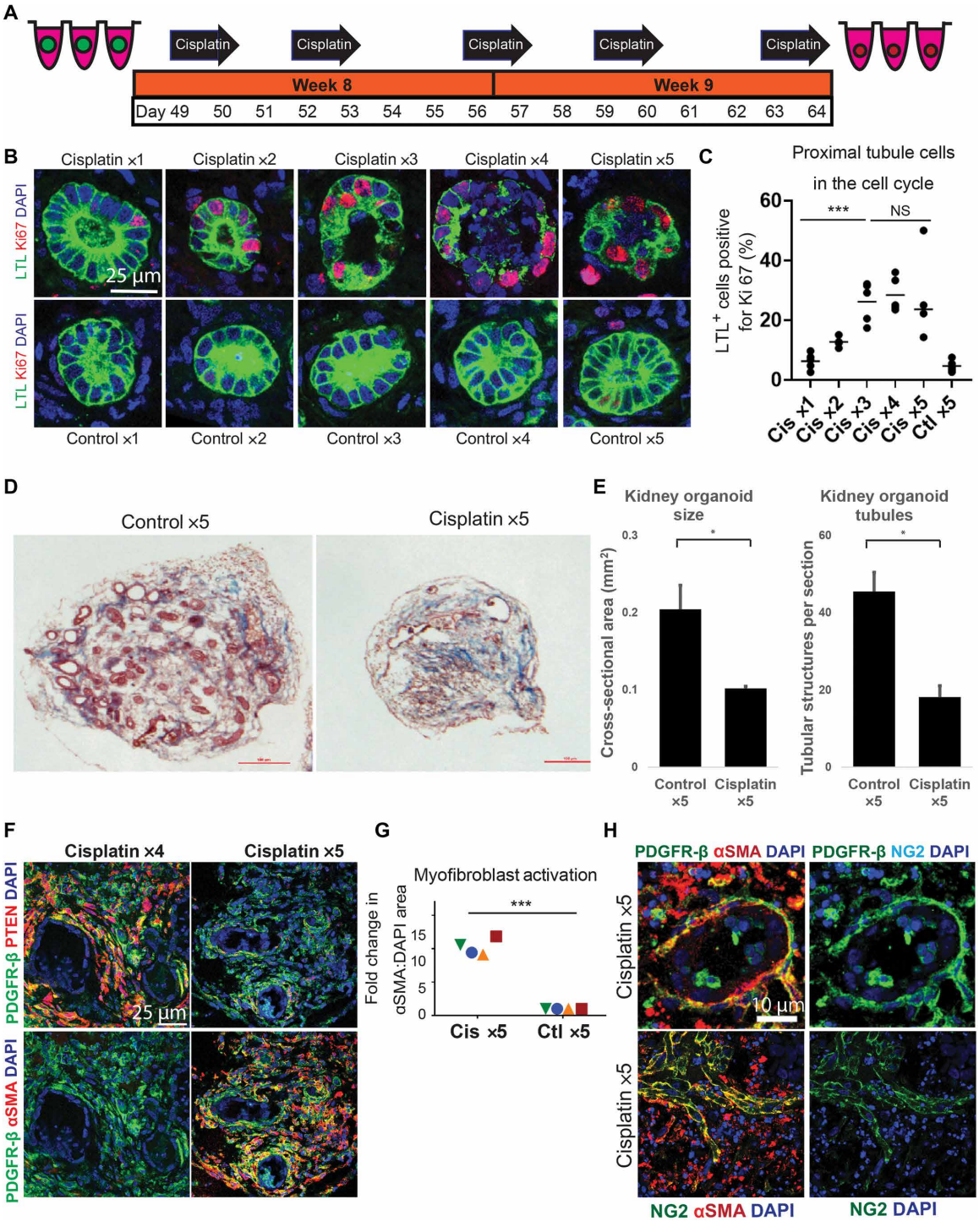

Fig. 3. Proximal tubular cells exhibit incomplete repair associated with tubular atrophy following repeated cisplatin treatment. (**A**) Experimental design for repeated cisplatin injury. (**B**) Ki67 and LTL immunostaining after repeated cisplatin exposure. Scale bar, 25 μm. (**C**) Quantification of Ki67$^+$ in LTL$^+$ cells after repeated cisplatin exposure. Each data point reflects the mean of three independent organoids in each of four independent experiments with a total of 3575 LTL$^+$ cells counted. (**D**) Masson trichrome staining of maximal diameter sections of cisplatin ×5–treated organoid compared to untreated control organoid. Scale bars, 100 μm. (**E**) Organoid size and tubular number in cisplatin ×5 compared to controls. The average horizontal and vertical measurements were averaged, radius was calculated, and cross-sectional area was determined by $A = \pi r^2$ ($P = 0.0221$). Number of tubular structures (right) using the average of two images per organoid and three total organoids per condition ($P = 0.0141$). (**F**) Immunostaining of PDGFR-β with PTEN or αSMA in cisplatin ×4 and ×5 samples. Scale bar, 25 μm. (**G**) αSMA/DAPI area after cisplatin ×5. Each symbol represents the mean of 20 randomly imaged fields, taken from four to six organoids per condition, from four independent experiments. (**H**) Top: PDGFR-β, αSMA, and NG2 immunostaining in cisplatin ×5; bottom: αSMA and NG2 immunostaining in cisplatin ×5. Scale bar, 10 μm. *$P < 0.05$ and ***$P < 0.001$.

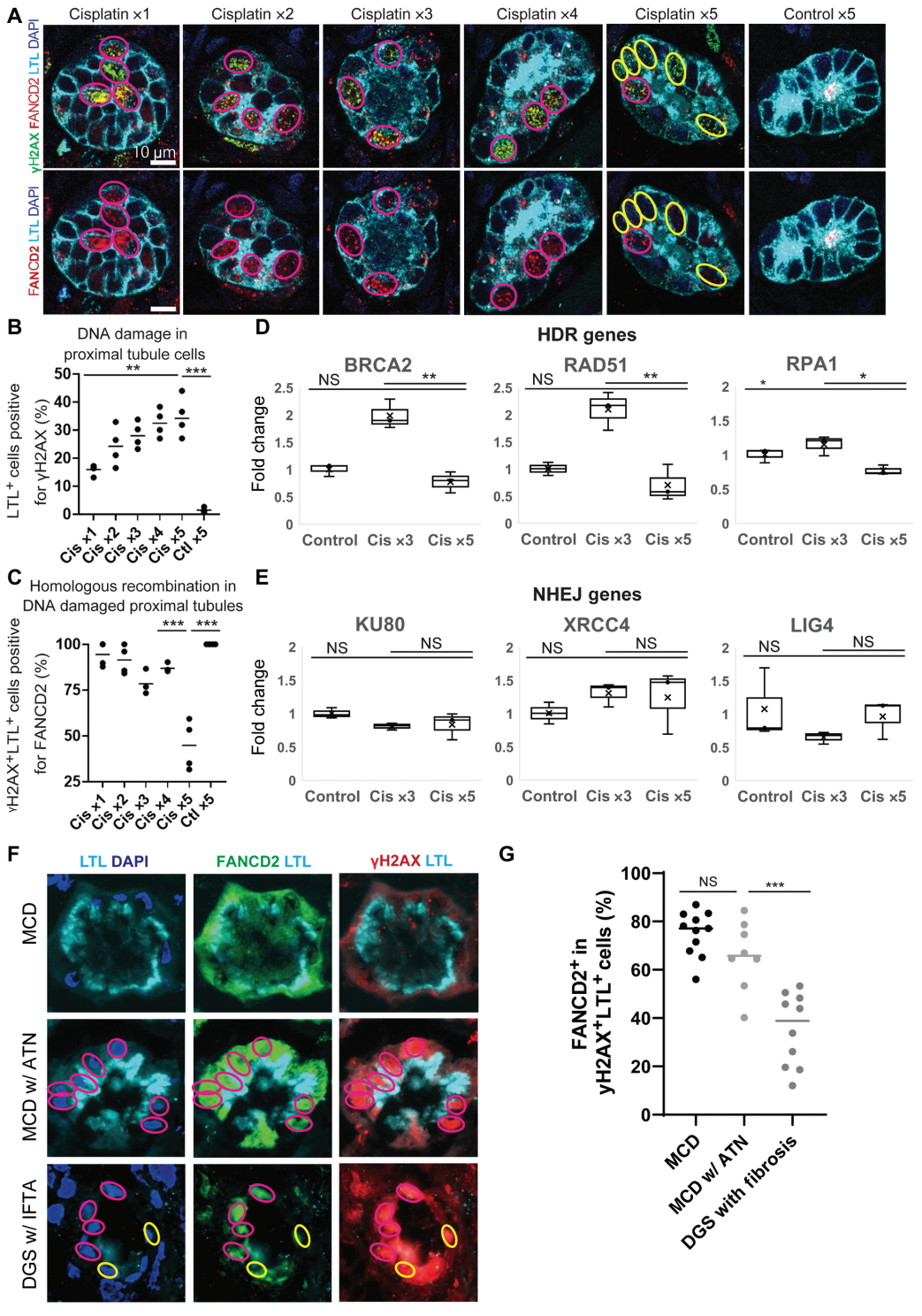

Fig. 4. Loss of HDR genes in injured tubular cells correlates with the induction of incomplete repair. (**A**) Immunostaining of γH2AX and FANCD2 in LTL^+ cells after repeated cisplatin exposure (pink circles outline double-positive cells, $\gamma H2AX^+FANCD2^+$, and yellow circles outline single positive cells, $\gamma H2AX^+FANCD2^-$). Scale bars, 10 μm. (**B**) Proportion of LTL^+ cells positive for γH2AX after repeated cisplatin exposure. Each data point reflects the mean value of three to five images from a minimum of three organoids in each of four experiments (2853 LTL^+ cells were counted). Cisplatin (Cis) ×5 versus control ×5 had *P* value of 9.366×10^{-5} and cisplatin ×1 versus cisplatin ×5 had *P* value of 0.00230. (**C**) $\gamma H2AX^+LTL^+$ cells positive for FANCD2 after repeated cisplatin exposure. Each data point reflects the mean value of three to five images from a minimum of three organoids in each of four experiments (483 $\gamma H2AX^+LTL^+$ cells were counted). Cisplatin ×4 versus cisplatin ×5 had *P* value of 8.76×10^{-4} and cisplatin ×5 versus control ×5 had *P* value of 1.86×10^{-4}. (**D**) RT-qPCR of HDR genes with repeated cisplatin. *BRCA2*: $P = 3.19 \times 10^{-3}$ (cisplatin ×3 versus cisplatin ×5) and 0.151 (control versus cisplatin ×5), *RAD51*: $P = 7.72 \times 10^{-3}$ (cisplatin ×3 versus cisplatin ×5) and 0.221 (control versus cisplatin ×5), and *RPA1*: $P = 3.20 \times 10^{-3}$ (cisplatin ×3 versus cisplatin ×5) and $P = 0.152$ (control versus cisplatin ×5). (**E**) RT-qPCR of NHEJ genes (*KU80*, *SRCC4*, and *LIG4*) after repeated cisplatin exposure. (**F**) LTL, FANCD2, and γH2AX immunostaining of kidney biopsies from patients with MCD, MCD with ATN, and DGS with IFTA (pink circles outline double positive cells, $\gamma H2AX^+FANCD2^+$, and yellow circles outline single positive cells, $\gamma H2AX^+FANCD2^-$). Scale bar, 25 μm. (**G**) $FANCD2^+$ in $\gamma H2AX^+LTL^+$ cells across human kidney biopsy samples. Each data point reflects results from the 9 to 11 independent patient samples per condition. $^*P < 0.05$, $^{**}P < 0.01$, and $^{***}P < 0.001$.

contamination from dead or dying cells while limiting stress-induced artifact from cellular dissociation (*52*). After quality control filtering with Cell Ranger (10X Genomics), the control yielded a mean of 121,557 reads from a median of 1401 genes, recorded in 4738 nuclei. Visualization of single-nucleus transcriptomes in uniform manifold approximation and projection (UMAP) space defined 12 clusters (fig. S9A). The proximity between tubular clusters (proximal tubules, distal tubules, and loop of Henle), podocyte clusters, and mesenchymal clusters reflects distance inversely correlating with transcriptional similarity in UMAP space (*53*). As previously described, cell-specific anchor genes were used to identify clusters, which included most nephron epithelia admixed with mesenchymal cells, muscle, and neurons (fig. S9B) (*52*).

A kidney organoid molecular atlas from basal state to intrinsic and incomplete repair phases was generated by snRNA-seq. After quality control filtering, 8278 nuclei were sequenced to a median depth of 1382 genes, reflecting a read depth similar to the control. Nuclei totaled 4738 in control, 2534 in intrinsic repair, and 1006 in incomplete repair samples, with cell death due to apoptosis after cisplatin treatment confirmed by cleaved caspase-3 immunostaining (fig. S10). Three new clusters were identified on UMAP clustering in intrinsic and incomplete repair phases, defined as injury 1, 2, and 3 (Fig. 5A). Injury clusters illustrated a gradual rightward shift in UMAP space and constituted the majority in both intrinsic and incomplete repair (Fig. 5, B and C). During the transition from intrinsic to incomplete repair, there was a reduction in injury cluster 2, whereas both injury clusters 1 and 3 increased (Fig. 5D). Although the control clusters were identified on the basis of accepted cell-specific markers, identification of the injury clusters was based on differentially expressed genes (DEGs), pathway analysis, and Gene Ontology (GO) analysis. On the basis of statistical significance, the top 50 DEGs in each injury cluster were derived (data files S1 to S3).

DEGs in injury cluster 1 included actin alpha 2 (ACTA2), collagen type I alpha 1 chain (COL1A1), and fibronectin 1 (FN1) (fig. S11A), whereas the top 3 GO terms reflected collagen and extracellular matrix (ECM) binding, activity, and constituents (Fig. 5E). These findings, coupled to the proximity of injury cluster 1 to mesenchyme in UMAP space (fig. 11B, top), suggest that this cluster represents myofibroblasts. Unbiased analysis of injury cluster 2 identified mouse double minute 2 (*MDM2*) as the top DEG. The human homolog of MDM2 monoubiquitinates p53, marking it for degradation in unstressed or reparative cells (*54*). Separate from its p53-binding domain, MDM2 binds to and delays DNA break repair machinery of NHEJ (*55*) while inhibiting p53-mediated suppression of HDR (*56*). *MDM2* expression appears to be a reparative phenotype with potentiated HDR. The top GO terms of injury cluster 2 included mitotic G1 DNA damage checkpoint (Fig. 5E). Coupling the reduction in injury cluster 2 with the transition from intrinsic to incomplete repair (Fig. 5D) with DNA damage, premitotic proliferative response (Fig. 5E), and the reparative phenotype of MDM2 (Fig. 5G), injury cluster 2 likely represents cells undergoing intrinsic repair.

Injury cluster 2 is composed of two subclusters, referred to as subcluster 2_1 and 2_2 hereafter (Fig. 5A). Despite disparate locations, the subclusters shared GO terms for "ECM," "ECM organization," "proteinaceous ECM," and "cell adhesion" in their top annotation cluster, underscoring their common designation. However, GO terms were attributed to *COL1A1* and *ACTA2* expression in subcluster 2_1 and *CTGF* and *TGF*-β expression in subcluster 2_2. On the basis of GO terms and location along the continuum from mesenchyme to myofibroblasts (fig. S11B, top), subcluster 2_1 was suggestive of activated stromal cells, including up-regulated *PTEN* expression consistent with our immunostaining (Fig. 3F). A feature plot of *ACTA2* reflects a continuum from low expression in mesenchyme 1 that increases to overlap with injury population 2, which further increases to manifest high expression in injury population 1 (fig. S11B, bottom). These findings suggested that peritubular fibroblasts of mesenchyme 1 transdifferentiate into myofibroblasts of injury 1 through a $PTEN^+$ intermediate of injury population 2_1. On the basis of continued expression of tubular epithelial solute transporters, *SLC3A2* and *SLC25A37*, coupled to its GO terms and location along the continuum from control proximal tubules to arrested cells manifesting incomplete repair (fig. S11B, top), subcluster 2_2 was suggestive of tubules undergoing intrinsic repair.

In injury cluster 3, the top two DEGs included cyclin-dependent kinase inhibitor 1A (*CDKN1A*; or p21) whose expression induces G_2-M arrest, an incomplete repair phenotype, in tubular cells (*57*). GO and BioCarta pathway analysis identified this population at the G_2-M checkpoint, while Kyoto Encyclopedia of Genes and Genomes pathway analysis revealed activation of the phosphoinositide 3-kinase/AKT pathway known to be activated by proximal tubular cells subject to cisplatin (*58*). Pathway analyses further demonstrated active p53 signaling based on *CDKN1A* and Bcl-2–associated X protein (*BAX*) expression. p53 induces apoptosis to protect against the propagation of cells carrying damaged DNA with potential oncogenic mutations (*54*), suggesting that injury cluster 3 represented cells injured beyond repair. In addition, the transforming growth factor–β and tumor necrosis factor pathways were active on GO analysis, indicating a proinflammatory phenotype. Injury cluster 3 therefore appeared to be composed of cells manifesting incomplete repair.

After putative identification, we determined HDR gene expression in the injury clusters. Bulk analysis of the snRNA-seq dataset demonstrated induction of HDR genes—*FANCD2*, *RPA1*, *RAD51*, and *BRCA2*—at the intrinsic repair phase, which reduced to below controls during incomplete repair (Fig. 5F). Meanwhile, the NHEJ genes of *Ku80*, *XRCC4*, and *LIG4* remained largely unchanged between intrinsic and incomplete repair (fig. S11C). Both the trend and magnitude of HDR gene expression support the reverse transcription qPCR results (Fig. 4D). Single cellular resolution reflected that injury cluster 2 was the primary driver of the changes in HDR genes (Fig. 5H). Subclustering demonstrated *FANCD2* and *BRCA2* expression localized to injury cluster 2_2 (Fig. 5I and fig. S11D). These data, along with the immunostaining of FANCD2 in LTL^+ tubules (Fig. 2, C and D), further identified the FANCD2-expressing injury cluster 2_2 as proximal tubules manifesting intrinsic repair (Fig. 5I).

Single cell transcriptomics confirms tubular HDR gene expression during intrinsic repair after hemodynamic, obstructive, and immune-mediated mammalian kidney injury

We next sought to determine whether the association between HDR gene expression and intrinsic repair was a generalizable finding beyond cisplatin-induced tubular damage. We therefore interrogated snRNA-seq datasets from mammalian kidney disease models. Unilateral ureteral obstruction (UUO) and ischemia-reperfusion injury are two common methods to model obstructive and hemodynamic mammalian kidney injury and identify intrinsic and incomplete repair phenotypes (*59*). A scRNA-seq dataset of rejecting human kidney transplant further permitted analysis of immune-mediated kidney injury (*27*).

The mouse UUO dataset included five distinct proximal tubular clusters, which included the S1, S2, and S3 segments seen in uninjured kidney and two UUO-induced clusters identified as proliferative and dedifferentiated proximal tubules (Fig. 6A). Proliferating proximal tubule characteristic of intrinsic repair exhibited the highest expression of *Mdm2* and associated genes of the homologous recombination complex, namely, *Fancd2*, *Brca2*, *Rad51*, and *Rpa1* (Fig. 6B). This proliferative population was termed the cycling proximal tubule cluster whose top DEGs of *Top2a* and *Cdca2* are

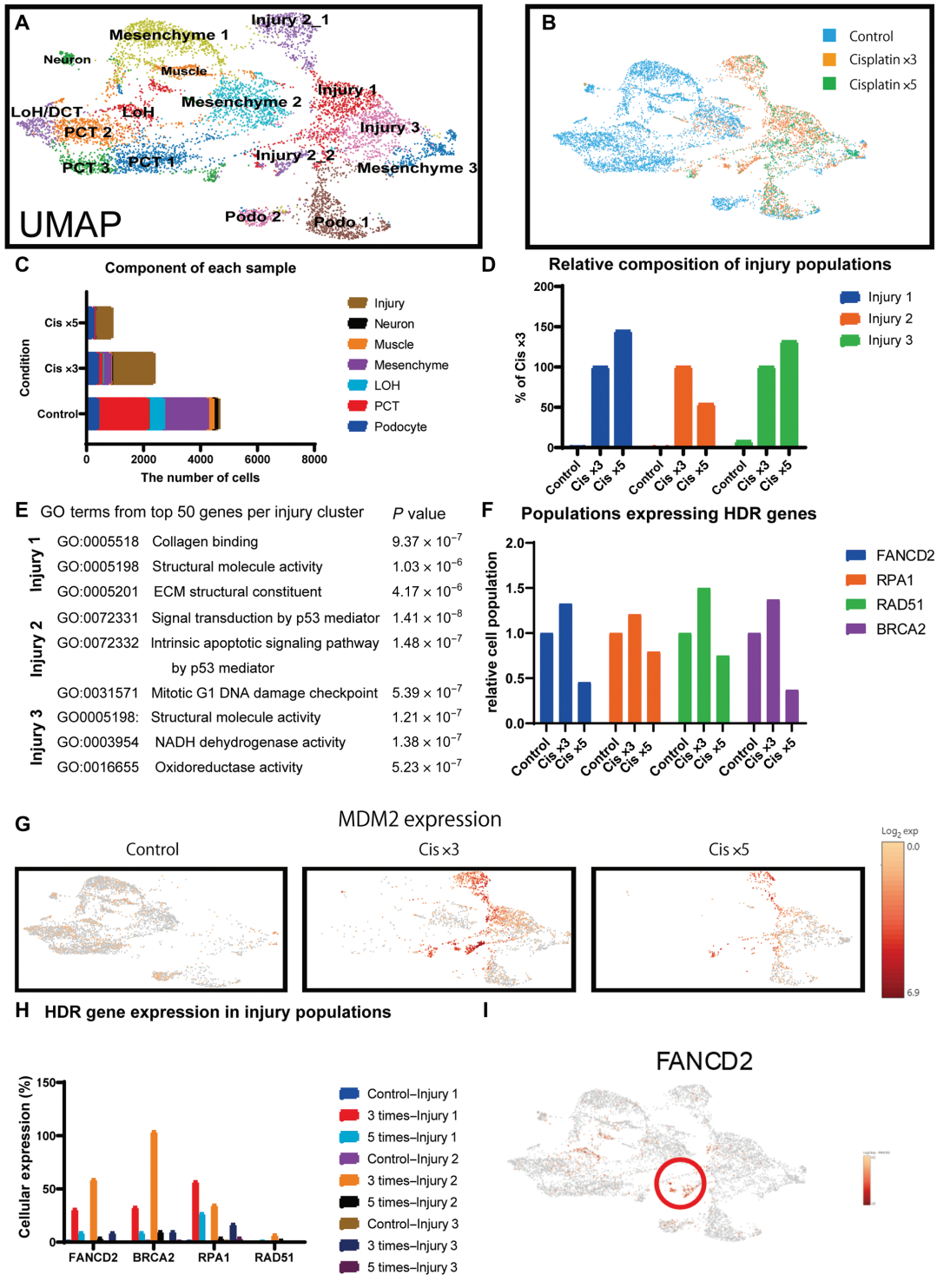

Fig. 5. snRNA-seq reveals injury clusters with HDR gene activity during intrinsic repair. (**A**) UMAP projection of superimposed 4738 control nuclei, 2534 cisplatin ×3 nuclei, and 1006 cisplatin ×5 nuclei. PCT, proximal convoluted tubule; LoH, loop of Henle; DCT, distal convoluted tubule; Podo, podocyte. (**B**) Differential contributions of control, intrinsic, and incomplete repair samples to the overall UMAP in (A), noting injury clusters 1, 2_1, 2_2, and 3. (**C**) Control, cisplatin ×3, and cisplatin ×5 samples by representation from each primary cellular cluster. (**D**) Representation of injury clusters in control, cisplatin ×3, and cisplatin ×5, standardized to cisplatin ×3. (**E**) Top 3 GO terms from injury clusters. (**F**) Bulk analysis of snRNA-seq for expression of HDR genes in control, cisplatin ×3, and cisplatin ×5. (**G**) *MDM2* expression in UMAP space from control, cisplatin ×3, and cisplatin ×5. (**H**) Single cellular resolution of HDR genes (*FANCD2*, *BRCA2*, *RPA1*, and *RAD51*). (**I**) UMAP projection of *FANCD2* expression, noting injury cluster 2_2 outlined by red circle.

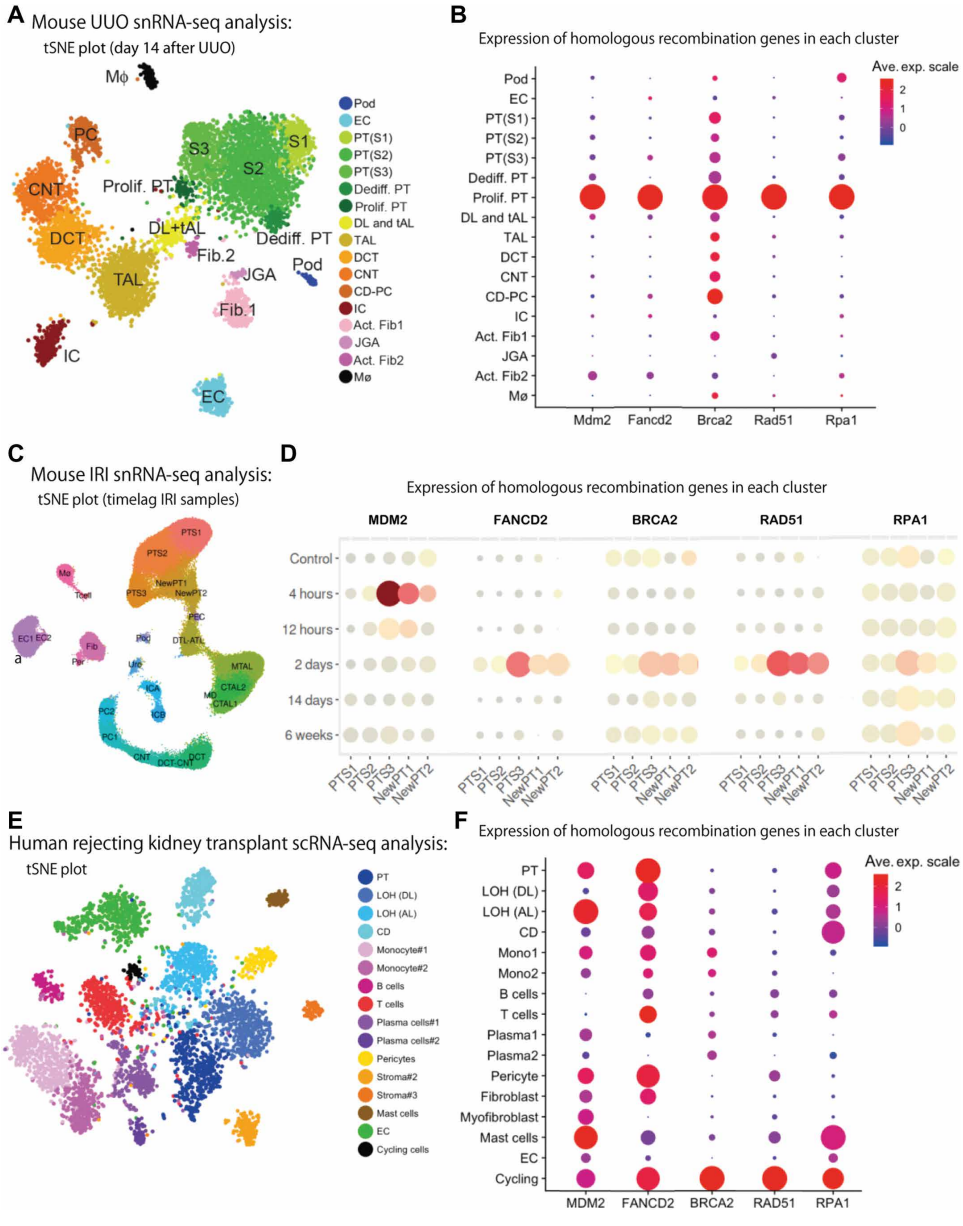

Fig. 6. Single-cell transcriptomics confirms tubular HDR gene expression during intrinsic repair after hemodynamic, obstructive, and immune-mediated mammalian kidney injury. (**A**) t-Distributed Stochastic Neighbor Embedding (tSNE) plot of a snRNA-seq dataset of mouse kidney 14 days after unilateral ureteral obstruction (UUO) identifying 17 separate cell clusters (*58*). (**B**) Gene expression of HDR-related genes across clusters in the mouse UUO dataset. (**C**) tSNE plot of an integrated snRNA-seq dataset of mouse kidney over time after ischemia-reperfusion injury (IRI) identifying five proximal tubule clusters (*13*). (**D**) Gene expression of HDR-related genes across clusters in the integrated mouse IRI dataset. (**E**) tSNE plot of a snRNA-seq dataset of human rejecting kidney transplant identifying 16 distinct cell clusters, PT is proximal tubule, DL is descending limb, AL is ascending limb, CD is collecting duct, and EC is endothelial cell (*27*). (**F**) HDR-related gene expression across clusters in the human rejecting kidney transplant dataset.

critical for the cellular division required for intrinsic repair (*52*), and transcriptional profiling of the two new injury clusters reflected derivation from proximal tubular cells. The transcriptome of new PT1 reflected intrinsic repair with concurrent expression of the tubular injury marker, *Hacv1*, and the reparative marker, *Bmp6* (*27*, *60*, *61*). New PT2, whose top DEGs included the incomplete repair marker *Vcam1* (*13*), was identified as the proinflammatory and profibrotic proximal tubular cell. Along a continuum from the basal state (PT3) to intrinsic repair (new PT1) and incomplete repair (new PT2), the expression of HDR-related genes was progressively reduced (Fig. 6D).

The human-rejecting kidney transplant dataset was generated from a patient with biopsy-proven mixed acute cellular rejection (ACR; Banff 1B) and acute antibody-mediated rejection in the setting of positive donor-specific antibodies. The rejecting proximal tubule cluster displayed a reduction of terminal differentiation markers and up-regulation of genes related to pro-inflammatory cytokines (*27*). In the setting of acute kidney rejection, associated with an injured proximal tubular phenotype, a proliferative cluster was identified and termed cycling (Fig. 6E). The cycling cluster expressed markers of active proliferation with *TOP2A*, *CENPF*, and *MKI67* as its top 3 DEGs, as well as *VIM*, consistent with an intrinsic repair phenotype that was associated with up-regulation of HDR-related genes (Fig. 6F). *VCAM1*$^+$ was used as an anchor gene to identify an incomplete repair cluster and so was not identified in an unbiased fashion. Despite this selection, *VCAM1* demonstrated its highest expression in the parietal epithelial cell (PEC) cluster in this human dataset, as well as in human snRNA-seq datasets of healthy kidney (n = 3), AKI (n = 6), and CKD (n = 10) from the kidney precision medicine project (https://atlas.kpmp.org/explorer/). *Vcam1* is poorly expressed in PECs in the mouse (fig. S12A), which signifies cross-species differential expression that may limit targeting VCAM1$^+$ cells for therapeutic purposes in humans. In both control and incomplete repair phase kidney organoids, *VCAM1* expression was limited to the parietal epithelial layer surrounding PODXL$^+$ cell clusters, consistent with PECs (fig. S12B).

FANCD2/RAD51-mediated DNA repair is a critical mediator of tubular intrinsic repair whose loss instigates tubular atrophy and myofibroblast activation

After confirming that HDR gene expression correlated with intrinsic repair across obstructive, hemodynamic, and immune-mediated kidney injury, we hypothesized that FANCD2/RAD51-mediated repair represented a mechanism governing intrinsic repair after kidney injury. To test this hypothesis, the repeated cisplatin injury

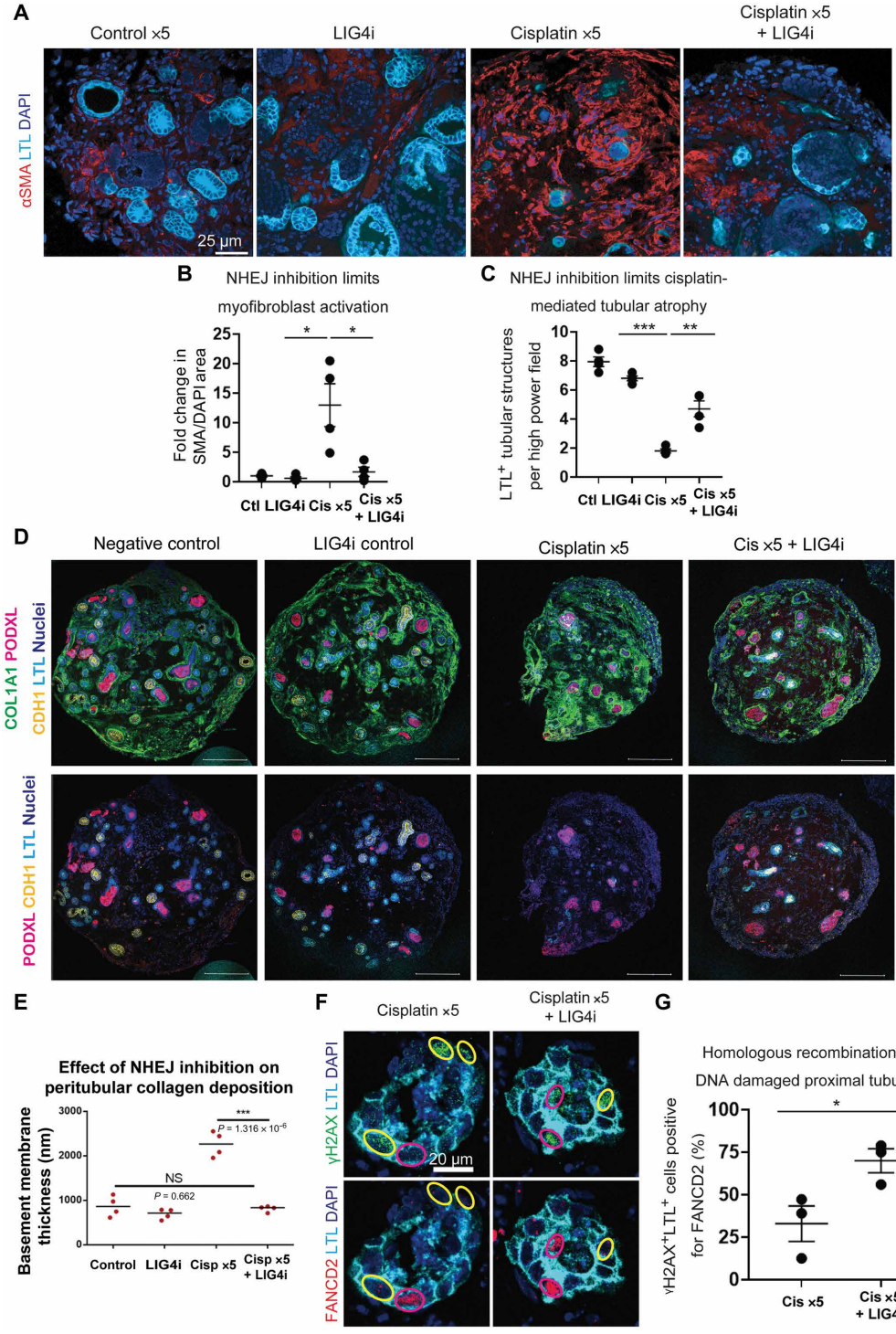

Fig. 7. Homologous recombination is a critical mediator of tubular intrinsic repair whose loss instigates tubular atrophy and myofibroblast activation. (**A**) Immunostaining of αSMA and LTL following cisplatin ×5 with inhibition of LIG4 compared to cisplatin alone. Scale bar, 25 μm. (**B**) Quantification of αSMA immunostaining after cisplatin ×5 with LIG4 inhibition compared to cisplatin alone. Ctl, control. (**C**) Quantification of LTL^+ tubules across samples. Each dot reflects the average of three images per organoid, from a minimum of three organoids, in four experiments. Cisplatin ×5 versus cisplatin ×5 + LIG4i had *P* value of 2.11×10^{-3} and LIG4i versus cisplatin ×5 had *P* value of 4.26×10^{-7}. Each dot reflects the average of three images per organoid, from a minimum of three organoids, in four experiments. Cisplatin ×5 versus cisplatin ×5 + LIG4i had *P* value of 0.0224 and LIG4i versus cisplatin ×5 had *P* value of 0.0143. (**D**) Immunostaining of nephron markers and COL1A1 in whole organoids. Scale bars, 200 μm. (**E**) Quantification of LTL^+ tubular basement membrane thickness across samples. $n = 2$ to 4 measurements in each of five LTL^+ tubular structures from four organoids per conditions. (**F**) FANCD2 and γH2AX immunostaining after cisplatin with and without LIG4 inhibition (pink circles outline double-positive cells, $\gamma H2AX^+FANCD2^+$, and yellow circles outline single-positive cells, $\gamma H2AX^+FANCD2^-$). Scale bar, 20 μm. (**G**) Quantification of FANCD2 in $\gamma H2AX^+LTL^+$ cells in cisplatin ×5 with and without LIG4 inhibition. Each data point represents the mean of three organoids in each of three independent experiments ($P = 0.0430$). *$P < 0.05$, **$P < 0.01$, and ***$P < 0.001$.

protocol (Fig. 3A) was performed under continuous inhibition of key HDR or NHEJ proteins. The strand exchange protein, RAD51, plays a central role in HDR. A 5′ degradation of DSBs generates 3′ overhangs flanking each side of the double-stranded defect. RAD51 binds the 3′ overhangs, forming a protein complex with FANCD2, BRCA1 DNA repair associated (BRCA1), and BRCA2 that facilitates the search for homologous sequences and, on identification, coordinates strand invasion for HDR (fig. S13A) (*62*). Downregulation of FANCD2-RAD51 is associated with decreased HDR events, suggesting that the FANCD2-RAD51 complex is essential for genomic preservation during DSB repair (*63*). After the third cisplatin injury in hPSC-derived kidney organoids, the presence of continuous RAD51 inhibition potentiated tubular atrophy and myofibroblast activation (fig. S13, B to D). In addition, inhibiting RAD51 exacerbated peritubular collagen type 1 (COL1) deposition (fig. S14, A and B), further indicating that loss of HDR for DSB repair potentiates incomplete repair processes. On the other hand, the blunt end ligation process of NHEJ is catalyzed by DNA ligase type IV (LIG4) (*64*). Proinflammatory cytokines have been demonstrated to induce DNA ligase type IV, thereby promoting the error-prone, DNA repair process of NHEJ (*65*, *66*). Unlike HDR, inhibition of LIG4 to prevent NHEJ did not exacerbate tubular atrophy, myofibroblast activation, or peritubular COL1 deposition (Fig. 7, A to E, and fig. S14C). Rather, LIG4 inhibition partially reversed kidney organoid atrophy (fig. S15, A and B) and rescued FANCD2 expression in DNA-damaged tubular cells (Fig. 7, D to G), consistent with previous work (*67*). The FANCD2/RAD51 complex therefore governed intrinsic repair in injured proximal tubules and preserved expression abrogated development of tubular atrophy and fibrosis characteristic of CKD.

DISCUSSION

Human stem cell–derived kidney tissue represents an emerging technology that may improve our understanding of pathophysiologic mechanisms for therapeutic development. The translational power of human kidney organoids will depend on their fidelity in approximating their in vivo counterparts and simulating diseased states. We have previously identified the epithelial derivatives of NPCs in kidney organoids, with functional demonstrations of nephrotoxicity testing and developmental modeling (*15*, *19*). Here, we identified the coinduction of a stromal progenitor pool with NPCs at the metanephric mesenchyme stage, which differentiate to form multicompartment kidney organoids that mature over time. Given the presence of tubular epithelial structures juxtaposed to stromal fibroblasts and pericytes, we sought to model epithelial and stromal incomplete repair processes known to induce irreversible derangement of tissue structure. Our results indicated that loss of HDR is a molecular switch that contributes to the transition from intrinsic to incomplete repair. Specifically, the degree of tubular atrophy, myofibroblast activation, and collagen deposition in the tubular basement membrane was inversely related to the abundance of tubular FANCD2 after tubular injury.

Animal models of incomplete repair in the kidney often incorporate an instigating epithelial injury that results in DNA damage, either through direct DNA toxicity (for example, cisplatin or aristolochic acid) or through the generation of genotoxic reactive oxygen species (aminoglycoside administration, ischemia reperfusion injury, or UUO) (*30*, *68*–*70*). The DNA damage response (DDR) mechanisms of cisplatin nephropathy may therefore extend to other causes of kidney injury. Diabetic kidney disease (DKD) is the most common etiology for end-stage renal disease (*71*), and biopsy samples of patients with DGS associated with IFTA have reduced tubular FANCD2, suggesting the generalizability of our finding beyond direct chemotherapy-induced DNA damage. The pathologic link between kidney organoids and patients' biopsy samples suggests the ability of hPSC-derived kidney tissue to model common clinical forms of nongenetic kidney disease. Recent work that has generated a model of diabetic vasculopathy in blood vessel organoids (*72*), which coupled with our group's vascularization of kidney organoids (*29*), may permit modeling of DKD (*73*). By comparing to scRNA-seq from patients with early evidence of DKD (*74*), the reliability of the transcriptome in an organoid model may be interrogated at the cellular and compartmental levels. Similarly, the chromatin histone modifications, DNA methylation, and noncoding RNAs that represent epigenetic mechanisms governing DKD (*75*) may be compared. Using kidney organoids, genetic manipulations may enhance our understanding of pathophysiologic mechanisms, and platform screening may aid in the development of therapeutics.

Limitations of the work presented here include the implementation of a fibrotic kidney model that is based on proximal tubular DNA damage, namely cisplatin treatment, noting a animal fibrotic model of UUO is not possible in kidney organoids. To address this limitation, we cited literature regarding proximal tubular DNA damage seen in various kidney injury models and used human kidney biopsy samples from the most common kidney injury, DKD, which reflected that loss of tubular FANCD2 is inversely correlated with kidney fibrosis. Although this correlation was made between kidney organoids and native human kidney tissue, functional studies such as glomerular filtration rates were limited with kidney organoids, suggesting the necessity of future studies to develop more advanced human kidney models and in vitro functional assays.

Processes of intrinsic and incomplete repair that follow proximal tubule injury were validated against published works. However, most of the previous literature was performed in animal models that may not translate to human disease. Whereas merely 3% of the 3.1–billion base pair (bp) human genome corresponds to coding regions, it shares only 85% sequence homology compared to mice (*76*). The resultant 14-million bp difference in coding regions, coupled to variability in noncoding areas, may contribute to the multitude of drugs deemed safe and efficacious during preclinical testing in mice, only to fail at a rate of 92% during clinical trials in humans (*77*). Tissue generated from hPSCs may not need to be identical to their in vivo equivalent, merely more reliable than current tools in reproducing human physiology. Here, we leverage kidney organoids to identify loss of FANCD2 in injured tubules as a molecular mechanism governing the transition from intrinsic to incomplete repair and demonstrate that FANCD2 rescue limits irreversible destruction of kidney tissue in response to severe injury.

MATERIALS AND METHODS

Study design

The overall objective and design of our study involved cisplatin treatments and observations of reversible and irreversible kidney injury in kidney organoids, with findings correlated to human kidney biopsy specimens and mouse snRNA-seq datasets. Kidney organoids were assigned randomly to experimental and control groups. No samples were excluded for sample analyses. Predefined study components

of sample size (power analysis) and rules for stopping data collection were not applicable. Replication was conducted on biologic replicates as written.

Cell culture

H9 (WiCell) human embryonic and BJFF.6 human-induced PSCs (Washington University) were maintained on hESC-qualified Geltrex-coated (Thermo Fisher Scientific) plates using StemFit Basic02 (Ajinomoto Co. Inc.) supplemented with FGF2 (10 ng/ml; PeproTech), as previously reported (*19*). hPSC lines were passaged weekly using Accutase (STEMCELL Technologies) for dissociation and Y27632 (Tocris) for adhesion.

Kidney organoid generation

Directed differentiation of hPSCs into kidney organoids has been published elsewhere (*18*). Briefly, hPSCs were differentiated into metanephric mesenchyme cells on day 8 by a three-step directed differentiation protocol. Metanephric mesenchyme was transferred into suspension culture in 96-well ultralow adhesion plates (Corning) and further differentiated into kidney organoids, as previously reported (*18*). Quality control measures of SIX2 immunostaining on day 8 of differentiation and CDH1, LTL, and PODXL immunostaining on day 21 were performed on all batches of kidney organoids to limit batch-to-batch heterogeneity. Kidney organoids were maintained in 200 μl of basal media consisting of Advanced RPMI (Thermo Fisher Scientific) and GlutaMAX (Thermo Fisher Scientific) in 96-well plates, as previously reported. Media changes were conducted three times weekly with removal of 90 μl and addition of 100 μl of fresh basal media until day 49. Thereafter, full exchanges occurred in all samples with the timing of cisplatin.

Supplemented factor exposure

Cisplatin

Cisplatin (Sigma-Aldrich, catalog no. 232120) was supplemented in basal media at a concentration of 5 μM when used.

B02

The RAD51 inhibitor, B02 (Millipore, catalog no. 553525), was supplemented in Advanced RPMI (ARPMI) at a concentration of 5 μM when used.

SCR7

The DNA ligase type IV inhibitor, SCR7 (Sigma-Aldrich, catalog no. SML1546), was supplemented in ARPMI at a concentration of 1 μM when used.

Bulk RNA-seq and data analysis

Total RNA was isolated from hPSCs (day 0), hPSC-derived NPCs (day 8), and organoids on days 21, 35, and 49 of differentiation. RNA integrity was assessed (RNA Nano 6000 Assay Kit, Bioanalyzer 2100, Agilent Technologies). Total RNA (400 ng) was used for library preparation using the NEBNext Ultra II RNA Library Prep Kit for Illumina (New England BioLabs, #E7775). Libraries were quantified using Qubit for mass concentration, LabChip for fragments distribution, and qPCR for molar concentration. The qualified RNA-seq libraries were run on NovaSeq 6000 S4 sequencers (Illumina). Downstream analysis was performed using Spliced Transcripts Alignment to a Reference (STAR) (v2.5), HTseq (v0.6.1), Cufflink, and our wrapped scripts. Differential expression was determined through DESeq2/edgeR. Reference genome and gene model annotation files were downloaded from genome website browser (National Center for Biotechnology Information/University of California Santa Cruz/Ensembl). Indices of the reference genome were built using STAR, and paired-end clean reads were aligned to the reference genome using STAR (v2.5). STAR used the method of maximal mappable prefix to generate precise mapping of junction reads. HTSeq v0.6.1 was used to count the reads mapped to each gene. Fragments per kilobase of transcript per million mapped reads (FPKM) of each gene, which assumes that the relative expression of a transcript is proportional to the number of complementary DNA fragments that originate from it, was calculated on the basis of the length of the gene and read counts mapped to this gene.

Transcriptome data from each sample were compared with transcription factors, as previously reported (www.informatics.jax.org/go/term/GO:0061005). Transcriptomic data obtained from each population were also compared with developing human kidney datasets (GSE66302). Heatmap was made by ExAtlas software (https://lgsun.irp.nia.nih.gov/exatlas/index.html). We clustered different samples using expression level FPKM to see the correlation using hierarchical clustering distance method with the function of heatmap, self-organization mapping, and *k*-means using silhouette coefficient to adapt the optimal classification with default parameters in R.

Immunostaining of kidney organoids

Organoid samples were washed with phosphate-buffered saline (PBS) and fixed for 1 hour in 250 μl of 4% paraformaldehyde (PFA; Electron Microscopy Sciences). Samples were washed with 1 ml of PBS three times and placed in 500 μl of 30% sucrose in PBS at 4°C overnight. The following day, organoids were placed in tissue-embedding molds (Polysciences Inc.) and embedded in optimal cutting temperature (Tissue-Tek), and frozen blocks were created using liquid nitrogen. Next, frozen sections (8 μm) were cut using a cryostat and stored at −20°C. Frozen sections were thawed to room temperature, washed with PBS three times, blocked using 5 weight % (wt %) donkey serum in PBS containing 0.3 wt % Triton X-100 for 1 hour, washed with PBS three times, and incubated with primary antibodies in antibody-diluting buffer [ADB; 1% bovine serum albumin (BSA), 1× PBS, and 0.3% Triton X-100] at room temperature for 2 hours. Samples were washed with PBS three times, incubated with Alexa Fluor secondary antibodies in ADB for 1 hour at room temperature, and washed with PBS three times. Samples were counterstained, mounted with VECTASHIELD with or without 4i,6-diamidino-2-phenylindole (DAPI) (Vector Laboratories), and sealed using a cover slip. When staining with LTL-biotin, a streptavidin/biotin blocking kit (Vector Laboratories, SP-2002) was used as per the manufacturer's protocol.

Single-nuclei preparation and sequencing

Nuclei were isolated with Nuclei EZ Lysis buffer (NUC-101, Sigma-Aldrich) supplemented with protease inhibitor (5892791001, Roche) and ribonuclease (RNase) inhibitor (N2615, Promega and AM2696, Thermo Fisher Scientific). Organoids were homogenized using a Dounce homogenizer (885302-0002; Kimble Chase) in 2 ml of ice-cold Nuclei EZ Lysis buffer and incubated on ice for 5 min with additional 2 ml of lysis buffer. The homogenate was filtered through a 30-mm strainer (43-50030-03; pluriSelect) and centrifuged at 500*g* for 5 min at 4°C. The pellet was resuspended, washed with 4 ml of buffer, and then incubated on ice for 5 min. After centrifugation, the pellet was resuspended in nuclei suspension buffer (1× PBS, 0.04% BSA, and 0.1% RNase inhibitor), filtered through a 5-μm strainer (43-50005-03;

pluriSelect), and counted. RNA from single nuclei were encapsulated, barcoded, and reverse-transcribed on a 10× Chromium Single Cell Platform (10× Genomics). The library was sequenced in NovaSeq SP-100. The Cell Ranger v3.0.1 pipeline (https://support.10xgenomics.com/single-cell-gene-expression/software/downloads/latest) performed sample demultiplexing, alignment (based on GRCh38 human genome assembly), filtering, unique molecular identifier (UMI) counting, single-cell 3′ end gene counting, and quality control using the manufacturer's parameters. Loupe browser was used to analyze and visualize the data. GO enrichment was analyzed using the DAVID Functional Annotation Tool v6.8 on DEGs. By applying Monocle3 and Seurat, pseudotime trajectories were unsuccessful in linking injury and control clusters.

snRNA-seq analysis

Top 50 DEGs in the three injury clusters were input into http://geneontology.org/, and GO enrichment analysis was performed for biological function and molecular function.

Statistical analysis

Box and whiskers plots were generated by the standard convention. Bar graphs are expressed as means ± SE. ImageJ was used for αSMA and DAPI areas. Quantification of γH2AX and FANCD2 was dependent on five discrete foci representing a positive cell (*78*). Quantification of Ki67 was based on speckled nuclear pattern constituting a positive cell. Quantification of KIM-1 was based on presence of luminal stain. Statistical analysis was performed in Excel and statistical significance by two-tailed Tukey's pairwise comparison tests. Significance (*P* value) is indicated with asterisks by the standard convention. Graphs are presented in GraphPad Prism.

SUPPLEMENTARY MATERIALS

www.science.org/doi/10.1126/scitranslmed.abj4772
Materials and Methods
Figs. S1 to S15
Tables S1 and S2
MDAR Reproducibility Checklist
Data files S1 to S4

View/request a protocol for this paper from *Bio-protocol*.

REFERENCES AND NOTES

1. N. R. Hill, S. T. Fatoba, J. L. Oke, J. A. Hirst, C. A. O'Callaghan, D. S. Lasserson, F. D. R. Hobbs, Global prevalence of chronic kidney disease – a systematic review and meta-analysis. *PLOS ONE* **11**, e0158765 (2016).
2. W. K. Han, V. Bailly, R. Abichandani, R. Thadhani, J. V. Bonventre, Kidney injury molecule-1 (KIM-1): A novel biomarker for human renal proximal tubule injury. *Kidney Int.* **62**, 237–244 (2002).
3. T. Kusaba, M. Lalli, R. Kramann, A. Kobayashi, B. D. Humphreys, Differentiated kidney epithelial cells repair injured proximal tubule. *Proc. Natl. Acad. Sci. U.S.A.* **111**, 1527–1532 (2014).
4. B. D. Humphreys, S. Czerniak, D. P. DiRocco, W. Hasnain, R. Cheema, J. V. Bonventre, Repair of injured proximal tubule does not involve specialized progenitors. *Proc. Natl. Acad. Sci. U.S.A.* **108**, 9226–9231 (2011).
5. B. D. Humphreys, M. T. Valerius, A. Kobayashi, J. W. Mugford, S. Soeung, J. S. Duffield, A. P. McMahon, J. V. Bonventre, Intrinsic epithelial cells repair the kidney after injury. *Cell Stem Cell* **2**, 284–291 (2008).
6. S. Lovisa, V. S. LeBleu, B. Tampe, H. Sugimoto, K. Vadnagara, J. L. Carstens, C. C. Wu, Y. Hagos, B. C. Burckhardt, T. Pentcheva-Hoang, H. Nischal, J. P. Allison, M. Zeisberg, R. Kalluri, Epithelial-to-mesenchymal transition induces cell cycle arrest and parenchymal damage in renal fibrosis. *Nat. Med.* **21**, 998–1009 (2015).
7. D. A. Ferenbach, J. V. Bonventre, Mechanisms of maladaptive repair after AKI leading to accelerated kidney ageing and CKD. *Nat. Rev. Nephrol.* **11**, 264–276 (2015).
8. L. Yang, T. Y. Besschetnova, C. R. Brooks, J. V. Shah, J. V. Bonventre, Epithelial cell cycle arrest in G2/M mediates kidney fibrosis after injury. *Nat. Med.* **16**, 535–543 (2010).
9. M. T. Grande, B. Sanchez-Laorden, C. Lopez-Blau, C. A. De Frutos, A. Boutet, M. Arevalo, R. G. Rowe, S. J. Weiss, J. M. Lopez-Novoa, M. A. Nieto, Snail1-induced partial epithelial-to-mesenchymal transition drives renal fibrosis in mice and can be targeted to reverse established disease. *Nat. Med.* **21**, 989–997 (2015).
10. R. Morizane, S. Fujii, T. Monkawa, K. Hiratsuka, S. Yamaguchi, K. Homma, H. Itoh, miR-34c attenuates epithelial-mesenchymal transition and kidney fibrosis with ureteral obstruction. *Sci. Rep.* **4**, 4578 (2014).
11. V. S. LeBleu, G. Taduri, J. O'Connell, Y. Teng, V. G. Cooke, C. Woda, H. Sugimoto, R. Kalluri, Origin and function of myofibroblasts in kidney fibrosis. *Nat. Med.* **19**, 1047–1053 (2013).
12. M. H. Little, P. Kairath, Does renal repair recapitulate kidney development? *J. Am. Soc. Nephrol.* **28**, 34–46 (2017).
13. Y. Kirita, H. Wu, K. Uchimura, P. C. Wilson, B. D. Humphreys, Cell profiling of mouse acute kidney injury reveals conserved cellular responses to injury. *Proc. Natl. Acad. Sci.* **117**, 15874–15883 (2020).
14. I. Loeffler, G. Wolf, Transforming growth factor-β and the progression of renal disease. *Nephrol. Dial. Transplant.* **29** (Suppl. 1), i37–i45 (2014).
15. R. Morizane, A. Q. Lam, B. S. Freedman, S. Kishi, M. T. Valerius, J. V. Bonventre, Nephron organoids derived from human pluripotent stem cells model kidney development and injury. *Nat. Biotechnol.* **33**, 1193–1200 (2015).
16. M. Takasato, P. X. Er, H. S. Chiu, B. Maier, G. J. Baillie, C. Ferguson, R. G. Parton, E. J. Wolvetang, M. S. Roost, S. M. Chuva de Sousa Lopes, M. H. Little, Kidney organoids from human iPS cells contain multiple lineages and model human nephrogenesis. *Nature* **526**, 564–568 (2015).
17. B. S. Freedman, C. R. Brooks, A. Q. Lam, H. Fu, R. Morizane, V. Agrawal, A. F. Saad, M. K. Li, M. R. Hughes, R. V. Werff, D. T. Peters, J. Lu, A. Baccei, A. M. Siedlecki, M. T. Valerius, K. Musunuru, K. M. McNagny, T. I. Steinman, J. Zhou, P. H. Lerou, J. V. Bonventre, Modelling kidney disease with CRISPR-mutant kidney organoids derived from human pluripotent epiblast spheroids. *Nat. Commun.* **6**, 8715 (2015).
18. R. Morizane, J. V. Bonventre, Generation of nephron progenitor cells and kidney organoids from human pluripotent stem cells. *Nat. Protoc.* **12**, 195–207 (2017).
19. R. Morizane, J. V. Bonventre, Kidney organoids: A translational journey. *Trends Mol. Med.* **23**, 246–263 (2017).
20. D. R. Lemos, M. McMurdo, G. Karaca, J. Wilflingseder, I. A. Leaf, N. Gupta, T. Miyoshi, K. Susa, B. G. Johnson, K. Soliman, G. Wang, R. Morizane, J. V. Bonventre, J. S. Duffield, Interleukin-1β activates a MYC-dependent metabolic switch in kidney stromal cells necessary for progressive tubulointerstitial fibrosis. *J. Am. Soc. Nephrol.* **29**, 1690–1705 (2018).
21. Y. Ikeda, Z. Sun, X. Ru, L. H. Vandenberghe, B. D. Humphreys, Efficient gene transfer to kidney mesenchymal cells using a synthetic adeno-associated viral vector. *J. Am. Soc. Nephrol.* **29**, 2287–2297 (2018).
22. N. O. Lindstrom, J. A. McMahon, J. Guo, T. Tran, Q. Guo, E. Rutledge, R. K. Parvez, G. Saribekyan, R. E. Schuler, C. Liao, A. D. Kim, A. Abdelhalim, S. W. Ruffins, M. E. Thornton, L. Basking, B. Grubbs, C. Kesselman, A. P. McMahon, Conserved and divergent features of human and mouse kidney organogenesis. *J. Am. Soc. Nephrol.* **29**, 785–805 (2018).
23. A. Kobayashi, J. W. Mugford, A. M. Krautzberger, N. Naiman, J. Liao, A. P. McMahon, Identification of a multipotent self-renewing stromal progenitor population during mammalian kidney organogenesis. *Stem Cell Reports* **3**, 650–662 (2014).
24. G. Bergers, S. Song, The role of pericytes in blood-vessel formation and maintenance. *Neuro Oncol.* **7**, 452–464 (2005).
25. L. L. O'Brien, Q. Guo, Y. Lee, T. Tran, J. D. Benazet, P. H. Whitney, A. Valouev, A. P. McMahon, Differential regulation of mouse and human nephron progenitors by the Six family of transcriptional regulators. *Development* **143**, 595–608 (2016).
26. E. W. Brunskill, J.-S. Park, E. Chung, F. Chen, B. Magella, S. S. Potter, Single cell dissection of early kidney development: Multilineage priming. *Development* **141**, 3093–3101 (2014).
27. H. Wu, A. F. Malone, E. L. Donnelly, Y. Kirita, K. Uchimura, S. M. Ramakrishnan, J. P. Gaut, B. D. Humphreys, Single-cell transcriptomics of a human kidney allograft biopsy specimen defines a diverse inflammatory response. *J. Am. Soc. Nephrol.* **29**, 2069–2080 (2018).
28. H. Wu, K. Uchimura, E. Donnelly, Y. Kirita, S. A. Morris, B. D. Humphreys, Comparative analysis and refinement of human PSC-derived kidney organoid differentiation with single cell transcriptomics. *Cell Stem Cell* **23**, 869–881 (2018).
29. K. A. Homan, N. Gupta, K. T. Kroll, D. B. Kolesky, M. Skylar-Scott, T. Miyoshi, D. Mau, M. T. Valerius, T. Ferrante, J. V. Bonventre, J. A. Lewis, R. Morizane, Flow-enhanced vascularization and maturation of kidney organoids in vitro. *Nat. Methods* **16**, 255–262 (2019).
30. R. P. Miller, R. K. Tadagavadi, G. Ramesh, W. B. Reeves, Mechanisms of Cisplatin nephrotoxicity. *Toxins* **2**, 2490–2518 (2010).
31. A. Ozkok, C. L. Edelstein, Pathophysiology of cisplatin-induced acute kidney injury. *Biomed. Res. Int.* **2014**, 967826 (2014).
32. M. Kruidering, B. Van de Water, E. de Heer, G. J. Mulder, J. F. Nagelkerke, Cisplatin-induced nephrotoxicity in porcine proximal tubular cells: Mitochondrial dysfunction by inhibition

of complexes I to IV of the respiratory chain. *J. Pharmacol. Exp. Ther.* **280**, 638–649 (1997).
33. J. Y. Soo, J. Jansen, R. Masereeuw, M. H. Little, Advances in predictive in vitro models of drug-induced nephrotoxicity. *Nat. Rev. Nephrol.* **14**, 378–393 (2018).
34. M. Kajiwara, T. Terada, K. Ogasawara, J. Iwano, T. Katsura, A. Fukatsu, T. Doi, K. Inui, Identification of multidrug and toxin extrusion (MATE1 and MATE2-K) variants with complete loss of transport activity. *J. Hum. Genet.* **54**, 40–46 (2009).
35. L. J. Kuo, L.-X. Yang, γ-H2AX - A novel biomarker for DNA double-strand breaks. *In Vivo* **22**, 305–309 (2008).
36. Y. Teng, M. Zeisberg, R. Kalluri, Transcriptional regulation of epithelial-mesenchymal transition. *J. Clin. Invest.* **117**, 304–306 (2007).
37. W. Kriz, B. Kaissling, M. Le Hir, Epithelial-mesenchymal transition (EMT) in kidney fibrosis: Fact or fantasy? *J. Clin. Invest.* **121**, 468–474 (2011).
38. S. Kumar, J. Liu, P. Pang, A. M. Krautzberger, A. Reginensi, H. Akiyama, A. Schedl, B. D. Humphreys, A. P. McMahon, Sox9 activation highlights a cellular pathway of renal repair in the acutely injured mammalian kidney. *Cell Rep.* **12**, 1325–1338 (2015).
39. A. Cano, M. A. Perez-Moreno, I. Rodrigo, A. Locascio, M. J. Blanco, M. G. del Barrio, F. Portillo, M. A. Nieto, The transcription factor snail controls epithelial-mesenchymal transitions by repressing E-cadherin expression. *Nat. Cell Biol.* **2**, 76–83 (2000).
40. G. Balmus, D. Pilger, J. Coates, M. Demir, M. Sczaniecka-Clift, A. C. Barros, M. Woods, B. Fu, F. Yang, E. Chen, M. Ostermaier, T. Stankovic, H. Ponstingl, M. Herzog, K. Yusa, F. M. Martinez, S. T. Durant, Y. Galanty, P. Beli, D. J. Adams, A. Bradley, E. Metzakopian, J. V. Forment, S. P. Jackson, ATM orchestrates the DNA-damage response to counter toxic non-homologous end-joining at broken replication forks. *Nat. Commun.* **10**, 87 (2019).
41. S. Hussain, J. B. Wilson, A. L. Medhurst, J. Hejna, E. Witt, S. Ananth, A. Davies, J.-Y. Masson, R. Moses, S. C. West, J. P. de Winter, A. Ashworth, N. J. Jones, C. G. Mathew, Direct interaction of FANCD2 with BRCA2 in DNA damage response pathways. *Hum. Mol. Genet.* **13**, 1241–1248 (2004).
42. M. A. Venkatachalam, J. M. Weinberg, W. Kriz, A. K. Bidani, Failed tubule recovery, AKI-CKD transition, and kidney disease progression. *J. Am. Soc. Nephrol.* **26**, 1765–1776 (2015).
43. C. N. Sharp, M. A. Doll, T. V. Dupre, P. P. Shah, M. Subathra, D. Siow, G. E. Arteel, J. Megyesi, L. J. Beverly, L. J. Siskind, Repeated administration of low-dose cisplatin in mice induces fibrosis. *Am. J. Physiol. Renal Physiol.* **310**, F560–F568 (2016).
44. I. Grgic, G. Campanholle, V. Bijol, C. Wang, V. S. Sabbisetti, T. Ichimura, B. D. Humphreys, J. V. Bonventre, Targeted proximal tubule injury triggers interstitial fibrosis and glomerulosclerosis. *Kidney Int.* **82**, 172–183 (2012).
45. O. H. Maarouf, A. Aravamudhan, D. Rangarajan, T. Kusaba, V. Zhang, J. Welborn, D. Gauvin, X. Hou, R. Kramann, B. D. Humphreys, Paracrine Wnt1 drives interstitial fibrosis without inflammation by tubulointerstitial cross-talk. *J. Am. Soc. Nephrol.* **27**, 781–790 (2016).
46. T. Scholzen, J. Gerdes, The Ki-67 protein: From the known and the unknown. *J. Cell. Physiol.* **182**, 311–322 (2000).
47. D. P. Basile, J. V. Bonventre, R. Mehta, M. Nangaku, R. Unwin, M. H. Rosner, J. A. Kellum, C. Ronco; ADQI XIII Work Group, Progression after AKI: Understanding maladaptive repair processes to predict and identify therapeutic treatments. *J. Am. Society of Nephrol.* **27**, 687–697 (2016).
48. S. Moghazi, E. Jones, J. Schroepple, K. Arya, W. McClellan, R. A. Hennigar, W. Charles O'Neill, Correlation of renal histopathology with sonographic findings. *Kidney Int.* **67**, 1515–1520 (2005).
49. H. Hricak, C. Cruz, R. Romanski, M. H. Uniewski, N. W. Levin, B. L. Madrazo, M. A. Sandler, W. R. Eyler, Renal parenchymal disease: Sonographic-histologic correlation. *Radiology* **144**, 141–147 (1982).
50. J. Zhou, L. Jia, Z. Hu, Y. Wang, Pharmacological inhibition of PTEN aggravates acute kidney injury. *Sci. Rep.* **7**, 9503 (2017).
51. C. Kuppe, M. M. Ibrahim, J. Kranz, X. Zhang, S. Ziegler, J. Perales-Patón, J. Jansen, K. C. Reimer, J. R. Smith, R. Dobie, J. R. Wilson-Kanamari, M. Halder, Y. Xu, N. Kabgani, N. Kaesler, M. Klaus, L. Gernhold, V. G. Puelles, T. B. Huber, P. Boor, S. Menzel, R. M. Hoogenboezem, E. M. J. Bindels, J. Steffens, J. Floege, R. K. Schneider, J. Saez-Rodriguez, N. C. Henderson, R. Kramann, Decoding myofibroblast origins in human kidney fibrosis. *Nature* **589**, 281–286 (2021).
52. H. Wu, Y. Kirita, E. L. Donnelly, B. D. Humphreys, Advantages of single-nucleus over single-cell RNA sequencing of adult kidney: Rare cell types and novel cell states revealed in fibrosis. *J. Am. Soc. Nephrol.* **30**, 23–32 (2019).
53. M. W. Dorrity, L. M. Saunders, C. Queitsch, S. Fields, C. Trapnell, Dimensionality reduction by UMAP to visualize physical and genetic interactions. *Nat. Commun.* **11**, 1537–1537 (2020).
54. U. M. Moll, O. Petrenko, The MDM2-p53 interaction. *Mol. Cancer Res.* **1**, 1001–1008 (2003).
55. C. M. Eischen, Role of Mdm2 and Mdmx in DNA repair. *J. Mol. Cell Biol.* **9**, 69–73 (2017).
56. S. A. Gatz, L. Wiesmüller, p53 in recombination and repair. *Cell Death Differ.* **13**, 1003–1016 (2006).
57. T. Koyano, M. Namba, T. Kobayashi, K. Nakakuni, D. Nakano, M. Fukushima, A. Nishiyama, M. Matsuyama, The p21 dependent G2 arrest of the cell cycle in epithelial tubular cells links to the early stage of renal fibrosis. *Sci. Rep.* **9**, 12059–12059 (2019).
58. G. P. Kaushal, V. Kaushal, X. Hong, S. V. Shah, Role and regulation of activation of caspases in cisplatin-induced injury to renal tubular epithelial cells. *Kidney Int.* **60**, 1726–1736 (2001).
59. M. Ruiz-Ortega, S. Rayego-Mateos, S. Lamas, A. Ortiz, R. R. Rodrigues-Diez, Targeting the progression of chronic kidney disease. *Nat. Rev. Nephrol.* **16**, 269–288 (2020).
60. A. Dendooven, O. van Oostrom, D. M. van der Giezen, J. Willem Leeuwis, C. Snijckers, J. A. Joles, E. J. Robertson, M. C. Verhaar, T. Q. Nguyen, R. Goldschmeding, Loss of endogenous bone morphogenetic protein-6 aggravates renal fibrosis. *Am. J. Pathol.* **178**, 1069–1079 (2011).
61. J.-d. Yan, S. Yang, J. Zhang, T.-h. Zhu, BMP6 reverses TGF-β1-induced changes in HK-2 cells: Implications for the treatment of renal fibrosis. *Acta Pharmacol. Sin.* **30**, 994–1000 (2009).
62. L. Krejci, V. Altmannova, M. Spirek, X. Zhao, Homologous recombination and its regulation. *Nucleic Acids Res.* **40**, 5795–5818 (2012).
63. R. S. Bindra, P. J. Schaffer, A. Meng, J. Woo, K. Maseide, M. E. Roth, P. Lizardi, D. W. Hedley, R. G. Bristow, P. M. Glazer, Down-regulation of Rad51 and decreased homologous recombination in hypoxic cancer cells. *Mol. Cell. Biol.* **24**, 8504–8518 (2004).
64. U. Grawunder, D. Zimmer, S. Fugmann, K. Schwarz, M. R. Lieber, DNA ligase IV is essential for V(D)J recombination and DNA double-strand break repair in human precursor lymphocytes. *Mol. Cell* **2**, 477–484 (1998).
65. H. Zhang, D. E. Kozono, K. W. O'Connor, S. Vidal-Cardenas, A. Rousseau, A. Hamilton, L. Moreau, E. F. Gaudiano, J. Greenberger, G. Bagby, J. Soulier, M. Grompe, K. Parmar, A. D. D'Andrea, TGF-β inhibition rescues hematopoietic stem cell defects and bone marrow failure in fanconi anemia. *Cell Stem Cell* **18**, 668–681 (2016).
66. M.-R. Kim, J. Lee, Y. S. An, Y. B. Jin, I.-C. Park, E. Chung, I. Shin, M. H. Barcellos-Hoff, J. Y. Yi, TGFβ1 protects cells from γ-IR by enhancing the activity of the NHEJ repair pathway. *Mol. Cancer Res.* **13**, 319–329 (2015).
67. T. Maruyama, S. K. Dougan, M. C. Truttmann, A. M. Bilate, J. R. Ingram, H. L. Ploegh, Increasing the efficiency of precise genome editing with CRISPR-Cas9 by inhibition of nonhomologous end joining. *Nat. Biotechnol.* **33**, 538–542 (2015).
68. Z. Ma, Q. Wei, G. Dong, Y. Huo, Z. Dong, DNA damage response in renal ischemia-reperfusion and ATP-depletion injury of renal tubular cells. *Biochim. Biophys. Acta* **1842**, 1088–1096 (2014).
69. Y. Y. Chen, J. G. Chung, H. C. Wu, D. T. Bau, K. Y. Wu, S. T. Kao, C. Y. Hsiang, T. Y. Ho, S. Y. Chiang, Aristolochic acid suppresses DNA repair and triggers oxidative DNA damage in human kidney proximal tubular cells. *Oncol. Rep.* **24**, 141–153 (2010).
70. M.-P. Mingeot-Leclercq, P. M. Tulkens, Aminoglycosides: Nephrotoxicity. *Antimicrob. Agents Chemother.* **43**, 1003–1012 (1999).
71. K. Azushima, S. B. Gurley, T. M. Coffman, Modelling diabetic nephropathy in mice. *Nat. Rev. Nephrol.* **14**, 48 (2018).
72. R. A. Wimmer, A. Leopoldi, M. Aichinger, N. Wick, B. Hantusch, M. Novatchkova, J. Taubenschmid, M. Hämmerle, C. Esk, J. A. Bagley, D. Lindenhofer, G. Chen, M. Boehm, C. A. Agu, F. Yang, B. Fu, J. Zuber, J. A. Knoblich, D. Kerjaschki, J. M. Penninger, Human blood vessel organoids as a model of diabetic vasculopathy. *Nature* **565**, 505–510 (2019).
73. R. Morizane, Modelling diabetic vasculopathy with human vessel organoids. *Nat. Rev. Nephrol.* **15**, 258–260 (2019).
74. P. C. Wilson, H. Wu, Y. Kirita, K. Uchimura, H. G. Rennke, P. A. Welling, S. S. Waikar, B. D. Humphreys, The single cell transcriptomic landscape of early human diabetic nephropathy. *bioRxiv* , 645424 (2019).
75. M. Kato, R. Natarajan, Epigenetics and epigenomics in diabetic kidney disease and metabolic memory. *Nat. Rev. Nephrol.* **15**, 327–345 (2019).
76. S. Batzoglou, L. Pachter, J. P. Mesirov, B. Berger, E. S. Lander, Human and mouse gene structure: Comparative analysis and application to exon prediction. *Genome Res.* **10**, 950–958 (2000).
77. I. W. Y. Mak, N. Evaniew, M. Ghert, Lost in translation: Animal models and clinical trials in cancer treatment. *Am. J. Transl. Res.* **6**, 114–118 (2014).
78. L. J. Mah, A. El-Osta, T. C. Karagiannis, γH2AX: A sensitive molecular marker of DNA damage and repair. *Leukemia* **24**, 679–686 (2010).

Acknowledgments: We thank J. V. Bonventre, J. A. Lewis, and E. P. Rhee for institutional support; S. J. Hill for insightful discussion and sharing antibodies; Y. Yoda for cell culture; L. Racusen of Johns Hopkins University for the HKC-8 cell line; and S. Jain and B. Humphreys at Washington University for BJFF.6 human-induced PSC line and Kidney Interactive Transcriptomics. **Funding:** The outlined work was supported by a National Institutes of Health (NIH) T32 fellowship training grant (DK007527 to N.G.), a Harvard Stem Cell Institute interdisciplinary grant (to N.G.), two Brigham and Women's Hospital Research Excellence Award (to N.G. and R.M.), a Cell Science Research Foundation Award (to K.H.), an NCATS UCLA CTSI KL2 grant (to M.Y.), a Cedars-Sinai CTSI Clinical Scholar Grant (to M.Y.), a Brigham and Women's Hospital Faculty Career Development Award (to R.M.), a Harvard Stem Cell Institute

Seed Grant (to R.M.), a DiaComp Pilot & Feasibility Program (to R.M.), an NIH DP2EB029388 award (to R.M.), and an NIH U01EB028899 grant (to R.M.). **Author contributions:** R.M., N.G., T. Matsumoto, K.H., E.G.S., .K.S., and M.Y. participated in the conceptualization of the study design. Methodology was determined by N.G. (repeated cisplatin injury), T. Matsumoto (snRNA-seq), K.H. (intrinsic repair monitoring), E.G.S. (initial cisplatin injury), P.G. (flow cytometry), T. Miyoshi (repeated cisplatin injury), N.T. (histopathology), M.Y. (histopathology), and R.M. (overall methodology and of each part). Data investigation and visualization were conducted by N.G., T. Matsumoto, K.H., E.G.S., N.T., M.Y., and R.M. Funding acquisition was from R.M. Project administration was by M.Y. and R.M. Supervision was conducted by N.G., M.Y., and R.M. The original draft of the manuscript was authored by N.G. and R.M. Subsequent editing and revisions were conducted by all authors. **Competing interests:** The authors declare that they have no competing interests. **Data and materials availability:** All data associated with this study are present in the paper or the Supplementary Materials. The accession number for the bulk RNA-seq data is DDBJ Sequence Read Archive (DRA): DRA010266. The Gene Expression Omnibus (GEO) accession number for the bulk-RNA sequencing data reported in Fig. 1 is GSE164648. The GEO accession number for the snRNA-seq data reported in Fig. 5 is GSE164647.

Submitted 28 May 2021
Resubmitted 14 October 2021
Accepted 14 January 2022
Published 2 March 2022
10.1126/scitranslmed.abj4772

Science Translational Medicine

Modeling injury and repair in kidney organoids reveals that homologous recombination governs tubular intrinsic repair

Navin GuptaTakuya MatsumotoKen HiratsukaEdgar Garcia SaizPierre GalichonTomoya MiyoshiKoichiro SusaNarihito TatsumotoMichifumi YamashitaRyuji Morizane

Sci. Transl. Med., 14 (634), eabj4772. • DOI: 10.1126/scitranslmed.abj4772

Fingering FANCD2 in tubular repair

The transition from acute kidney injury, characterized by intrinsic repair, to incomplete repair and chronic damage has been difficult to study. Here, Gupta and colleagues modeled the transition from intrinsic to incomplete repair using human kidney organoids. A single exposure to cisplatin resulted in intrinsic repair, with preserved tubular architecture and up-regulation of genes associated with homology-directed repair, including Fanconi anemia complementation group D2 (*FANCD2*). However, with repeated cisplatin exposure, *FANCD2* and RAD51 recombinase (*RAD51*) were down-regulated, leading to incomplete repair. The DNA ligase IV inhibitor SCR7 increased FANCD2-mediated repair and ameliorated progression to chronic injury in the organoids, suggesting that targeting the FANCD2/RAD51 pathway may have potential to treat kidney disease.